

Phase shifting, dispersion variation and defocusing suppression in wave breaking

Anatoliy Khait[†] and Zhihua Ma[‡]

Centre for Mathematical Modelling and Flow Analysis, Department of Computing and Mathematics, Manchester Metropolitan University, Chester Street, Manchester M1 5GD, UK

(Received xx; revised xx; accepted xx)

We present an investigation of the fundamental physical processes involved in deep water wave breaking. Our motivation is to identify the underlying reason causing the deficiency of the eddy viscosity breaking model (EVBM) in predicting surface elevation for strongly nonlinear waves. Owing to the limitation of experimental methods in the provision of high-resolution flow information, we propose a numerical methodology by developing an EVBM enclosed standalone fully-nonlinear quasi-potential (FNP) flow model and a coupled FNP plus Navier-Stokes flow model. The numerical models were firstly verified with a wave train subject to modulational instability, then used to simulate a series of broad-banded focusing wave trains under non-, moderate- and strong-breaking conditions. A systematic analysis was carried out to investigate the discrepancies of numerical solutions produced by the two models in surface elevation and other important physical properties. It is found that EVBM predicts accurately the energy dissipated by breaking and the amplitude spectrum of free waves in terms of magnitude, but fails to capture accurately breaking induced phase shifting. The shift of phase grows with breaking intensity and is especially strong for high wavenumber components. This is identified as a cause of the upshift of wave dispersion relation, which increases the frequencies of large wavenumber components. Such a variation drives large-wavenumber components to propagate at nearly the same speed, which is significantly higher than the linear dispersion levels. This suppresses the instant dispersive spreading of harmonics after the focal point, prolonging the lifespan of focused waves and expanding their propagation space.

Key words: surface gravity waves, wave breaking, non-potential effects, phase shift

1. Introduction

Wave breaking is a highly important and challenging topic in engineering and environmental science. Violent breaking waves can produce destructive loads causing severe damage to, and even complete failure/loss of naval, coastal and marine structures including ships, breakwaters, seawalls, and oil and gas platforms (Babanin 2011; Ma *et al.* 2014, 2016). More broadly, wave breaking plays a crucial role in the planetary-scale atmosphere-ocean system by enhancing the exchange of mass, momentum and heat across the air-sea interface, thus influencing the earth's climate and weather (Kiger & Duncan 2012; Veron 2015). Breaking is also a major mechanism to dissipate wave energy,

[†] Email address for correspondence: haitanatoliy@gmail.com

[‡] Email address for correspondence: z.ma@mmu.ac.uk

preventing the endless growth of wind waves (Melville 1996). Breaking wave models, in particular the accurate estimate of energy dissipated through the process, constitute a key part of numerical ocean wave forecast, which is essential to the safety of maritime activities including, but not limited to, fishery, ship navigation and offshore construction and operation.

Despite the vast amount of theoretical, experimental and numerical work reported in the past, the fundamental mechanism of wave breaking has not been understood thoroughly yet due to its extraordinary complexity. Wave breaking is a multi-scale and multi-phase problem, which involves multiple orders of scales ranging from the large orbital motions induced by surface water waves to the small air bubbles entrained into water mass and spray ejected into the atmosphere. To fully resolve the transient flow features of breaking waves in numerical simulations, extremely fine meshes and small time steps are needed. However, this will place a prohibitive burden on computing resources, restricting the computational domain of high-fidelity numerical models to only several representative wave lengths for 3D problems (Iafrazi 2009; Lubin & Glockner 2015; Deike *et al.* 2017).

It is known that the onset of breaking and the post-breaking evolution of wave field are dependent on the breaking crest formation process, which is usually highly nonlinear (Khait & Shemer 2018). The development of breaking wave crest involves significantly large temporal and spatial scales that cannot be efficiently handled by high-fidelity numerical models alone yet (De Vita *et al.* 2018; Iafrazi *et al.* 2019). To effectively deal with these large scales, it is necessary to use low-fidelity models such as the potential model which assumes the flow to be inviscid and irrotational. Under such an approximation, the flow velocity can be calculated as the gradient of the potential function. Although the potential approximation allows a substantial simplification of the problem, it disregards the crucial physical effects such as fluid viscosity, flow vorticity and two-phase features for wave breaking problems. Empirical closures are thus needed to take into account these important effects in the evolution of wave field subject to breaking.

Chalikov & Sheinin (2005) noticed that the free surface close to an unstable crest became nearly vertical upon the inception of breaking, and high wavenumber spectral harmonics, accompanied by the nonlinear flux of energy from low to high wavenumbers, were generated. Damping the high wavenumber components of the spectrum and therefore dissipating the associated energy can help to stabilise the computation (Chalikov & Sheinin 2005; Chalikov & Babanin 2014). The damping process was actually accomplished by introducing empirical terms to the free surface boundary conditions. Similar approaches can be found in the extended High-Order Spectral Models of Ducrozet *et al.* (2012, 2016). For spectral ocean forecasting models, the nonlinear evolution of waves is considered as an energy cascade that transfers energy between different frequency harmonics. It allows to take into account the spectral energy dissipation due to breaking by using observation-based empirical source terms to parameterise the reduction of spectral components (Babanin *et al.* 2011; Annenkov & Shrira 2018).

Although damping high frequency spectral components is computationally efficient, this kind of method has inherent restrictions. One significant difficulty is that wave breaking cannot be adequately described in the Fourier space because it is strongly localised in the physical space. An alternative semi-empirical closure for wave breaking was proposed by Tian *et al.* (2010, 2012). This model contains only one empirical constant as opposed to numerous fitting parameters used in other breaking approximations. Therefore, it is preferable for studying breaking processes at large spatial and temporal scales. A number of researchers have demonstrated this model's accuracy and robustness

in the prediction of energy flux reduction for spilling and plunging breakers (Tian *et al.* 2010, 2012; Seiffert *et al.* 2017; Seiffert & Ducrozet 2018; Hasan *et al.* 2019; Craciunescu & Christou 2020). However, notable disagreements with experimental measurements in terms of the surface elevation for strongly-nonlinear wave trains have also been reported in the literature (Tian *et al.* 2012; Seiffert & Ducrozet 2018). The underlying reason causing the discrepancy between the eddy viscosity model and laboratory experiments remains unclear.

This requests further investigation to identify the actual cause by producing a series of realistic wave breaking scenarios and analysing a considerable amount of detailed flow data. However, state-of-the-art laboratory facilities, in particular measurement equipment, are still deficient in the provision of needed large amount of high-resolution spatial and temporal flow information. To circumvent these restrictions, a hybrid low- and high-fidelity numerical model is developed and applied in the present work. We coupled a boundary element method (BEM) based fully nonlinear quasi-potential (FNP) model with a volume-of-fluid method (VOF) based two-phase incompressible Navier-Stokes (NS) model to formulate the hybrid FNP-NS model. This new approach is used to deal with the generation, propagation and breaking of deep water waves and their post-breaking evolution. The accuracy of the numerical model is carefully assessed through a breaking wave train subject to modulational instability. The computed results are compared against the laboratory measurements and other numerical solutions reported in the literature. The FNP-NS model is then used to simulate the evolution of six broad-banded wave trains under non-, moderate- and strong-breaking conditions. The standalone FNP model, incorporated with the eddy viscosity enclosure, is also applied to compute these wave trains. This allows us to perform a comprehensive comparative study of breaking waves with the standalone FNP model and the hybrid FNP-NS model to quantify the deviations in surface elevation, energy dissipation and other important physical properties. Close attention is paid to the phases of free waves, the dispersion relationship between wavenumber and frequency, the trajectory of wave trains and their height before, during and after focusing. Detailed analyses of these important properties are carried out to examine the fundamental physical processes involved in breaking.

The remainder of the paper is organised as follows. The numerical methodology is described in Section 2 and carefully validated against wave flume experiments in Section 3. A detailed analysis of the wave train evolution observed in numerical simulations is presented in Sections 4.1 and 4.2. The breaking induced phase shifting phenomenon and variation of wave train dispersion are discussed in Sections 4.3 and 4.4. Section 4.5 is devoted to the discussion of the suppression of dispersive defocusing and associated processes. Conclusions are drawn and practical implications are discussed in Section 5.

2. Methodology

To reproduce realistically the generation, propagation and breaking of surface waves as well as their afterwards evolution, a number of numerical approaches are applied in the present work. This includes a fully-nonlinear potential flow (FNP) model and a two-phase incompressible viscous Navier-Stokes (NS) model. A hybrid FNP-NS approach is developed by connecting the FNP and NS models through a one-way coupling strategy (see Figure 1). Firstly waves are generated and propagated in the domain of the FNP model. The NS model is initialised after a certain amount of time when the waves arrive at its inlet boundary. Free surface elevation and flow velocity computed by the FNP model at the coupling boundary are then transferred to the NS model (see more details in Section 2.3).

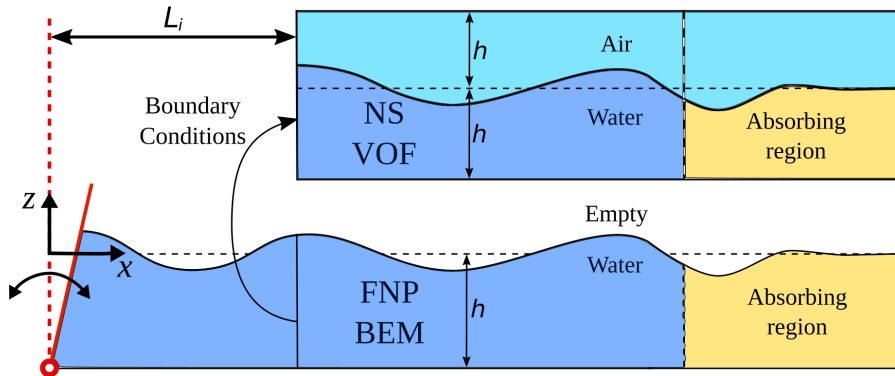


FIGURE 1. Schematic of the coupled FNP-NS model. Boundary Element Method (BEM) is used to discretise the FNP domain. Volume-of-Fluid (VOF) method is used to discretise the NS domain. In the present work we also use ‘BEM’ and ‘VOF’ to refer to the low- and high-fidelity flow models, respectively.

As mentioned above, the FNP model is efficient for large-scale problems but ignores important physical effects. On the contrary, the NS model includes important physical effects and provides more detailed flow information at the cost of computational efficiency. The coupled FNP-NS model provides a way to balance low- and high-fidelity computations. Another benefit of using the coupled model is that it can produce more realistic scenarios without introducing artificial conditions for wave breaking (Lubin & Glockner 2015).

In the present work we focused on two-dimensional wave breaking problems. A series of numerical computations of breaking events under different wave conditions were carried out by using the standalone FNP model and the coupled FNP-NS model, respectively. Detailed descriptions of the FNP and NS models are given in the following.

2.1. Fully-nonlinear quasi-potential model (BEM)

Under the potential approximation, the velocity field $\mathbf{U} = \{u, w\}$ is given by the gradient of the hydrodynamic potential φ , i.e. $\mathbf{U} = -\nabla\varphi$. The Boundary Element Method (BEM) is used to determine the distribution of φ across the FNP domain (Grilli *et al.* 1989; Grilli & Svendsen 1990). In this approach, the fluid flow is governed by the Green’s second identity:

$$\alpha\varphi(\mathbf{r}_s) = \oint_{\Gamma} \left(\frac{\partial\varphi}{\partial n}(\mathbf{r})\Phi(\mathbf{r}, \mathbf{r}_s) - \varphi(\mathbf{r})\frac{\partial\Phi}{\partial n}(\mathbf{r}, \mathbf{r}_s) \right) d\Gamma \quad (2.1)$$

Here $\Phi(\mathbf{r}, \mathbf{r}_s) = -1/(2\pi)\ln|\mathbf{r}-\mathbf{r}_s|$ is the fundamental solution that represents the potential flow at point \mathbf{r} due to a source located at \mathbf{r}_s ; Γ is the closed boundary of the domain; $\alpha = \pi$ for regular nodes, and $\alpha = \pi/2$ for corner nodes; n is the outward normal direction to Γ . The solution of (2.1) provides the value of $\partial\varphi/\partial n$ or φ at the point \mathbf{r} located on Γ . The 3rd-order MII local interpolation technique (Grilli & Subramanya 1996) was used to discretise the boundary Γ for numerical solution of (2.1).

The free surface is subject to the dynamic and kinematic boundary conditions determining the time variation of its shape. Since we investigate strongly breaking wave field, the inclusion of empirical closures in the FNP model is required to stabilise the computation. For weakly-damped waves (Ruvinsky *et al.* 1991), assuming the flow to be quasi-potential with small vortical velocity components, we can obtain the modified

TABLE 1. Parameters of the BEM model. Details on the wave trains studied are presented in Section 2.4; λ_0 is the carrier wave length.

	Gaussian wave train	Modulated wave train
Length of the domain	$26\lambda_0$	$31\lambda_0$
Still water depth h	0.6 m	3.0 m
Length of the absorbing region		$7\lambda_0$
Free surface grid resolution		30 nodes per λ_0
Bottom boundary resolution		20 nodes per λ_0

boundary conditions (Dias *et al.* 2008; Dosaev *et al.* 2021) given by:

$$\frac{D\mathbf{r}}{Dt} = -\nabla\varphi - \underbrace{\nabla \times \Psi}_{\text{wave breaking}} \quad (2.2)$$

$$\frac{D\varphi}{Dt} = gz - \frac{1}{2}|\nabla\varphi|^2 - \underbrace{\tilde{p}_d \sqrt{gh} \frac{\partial\varphi}{\partial n} b_f(x)}_{\text{wave absorption}} + \underbrace{2\nu_{eddy} \frac{\partial^2\varphi}{\partial s^2}}_{\text{wave breaking}} \quad (2.3)$$

The vector stream function $\Psi = (0, 0, \psi)$ contains only a vortical part of the flow; ν_{eddy} is the closure constant for the wave breaking model; s is the direction tangential to the free surface. The value of the stream function at the free surface is governed by the vorticity equation. The exact form of this equation cannot be satisfied for potential flows, therefore its approximate version is used (Ruvinsky *et al.* 1991; Dosaev *et al.* 2021):

$$\frac{\partial}{\partial t} \frac{\partial\psi}{\partial s} = 2\nu_{eddy} \frac{\partial^2}{\partial s^2} \frac{\partial\varphi}{\partial n}, \quad (2.4)$$

where $\partial\varphi/\partial n$ is the solution of (2.1). Equation (2.3) is also responsible for wave absorption at the end of the domain, see Figure 1. The dimensionless constant \tilde{p}_d characterises the strength of the wave damping; function $b_f(x)$ determines the location of the absorption region and the gradual increase of the damping strength in the beginning of the region. The most effective absorption occurs when $\tilde{p}_d = 2$ (Khait & Shemer 2018, 2019b).

The non-penetration condition $\partial\varphi/\partial n = 0$ is applied at the bottom and right boundaries. Moving boundary with specified velocity is introduced at the left side of the domain to replicate the motion of a wave paddle, see Figure 1. The domain size and grid resolution used in the simulations are summarised in Table 1. Grid convergence study is presented in Appendix A. Integration time step was taken to satisfy the numerical stability criterion defined by the Courant number $CFL \leq 0.1$ (Grilli & Svendsen 1990).

Two approaches namely regridding and empirical eddy viscosity for approximating the energy dissipation due to wave breaking are considered in the paper. First, it was found that regridding the free surface mesh at the instant of breaking inception can stabilise the numerical simulation without using the eddy viscosity closure, i.e. $\nu_{eddy} = 0$ in (2.2) and (2.3). For convenience, this model is designated as ‘BEMr’ in the following.

The grid nodes at the free surface represent the floating Lagrangian markers having all degrees of freedom. The distance between two neighbouring nodes is constantly varying due to the propagation of nonlinear waves. The regridding method developed by Subramanya & Grilli (1994) establishes equal lengths of the arcs between all neighbour nodes as measured along the boundary elements. At the instance of breaking inception,

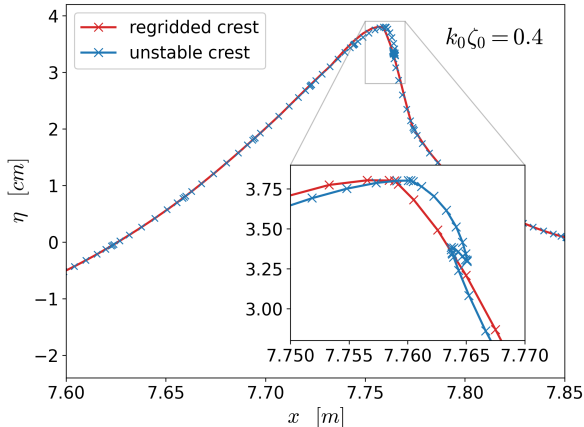


FIGURE 2. Shape of the pre-breaking wave crest before and after re-meshing. Cross markers show the mesh nodes on the free surface.

the distance between the nodes at the pre-breaking crest becomes critically small leading to consequent crest overturning and loss of computation stability. The shape of the pre-breaking crest with and without regridding is shown in Figure 2. It can be seen that the regridding method smoothens the shape of the pre-breaking crest and removes the unstable overturning part.

A more advanced approximation for wave breaking energy dissipation is based on the eddy viscosity empirical closure suggested by Tian *et al.* (2010, 2012). According to this method, the location of the breaking crest is established by using the geometrical criterion $S_b \geq S_c$; where S_b is the local free surface slope, while its threshold value is $S_c = 0.95$. Once the location of the breaking is determined, the eddy viscosity value is calculated by using the empirical relation (Tian *et al.* 2010, 2012):

$$\nu_{eddy} = \alpha \frac{H_b L_b}{T_b} \quad (2.5)$$

Here H_b and L_b are the characteristic vertical and horizontal scales of the breaking event, respectively, while T_b is the characteristic time scale. All these values are determined by using the empirical relations:

$$\begin{aligned} L_b &= \frac{24.3S_b - 1.5}{k_b} \\ T_b &= \frac{18.4S_b + 1.4}{\omega_b} \\ H_b &= \frac{0.87R_b - 0.3}{k_b} \end{aligned} \quad (2.6)$$

Here k_b and ω_b are the local wave parameters; R_b is the geometrical factor showing vertical asymmetry of the breaking wave crest. The value of the proportionality constant in (2.5) is $\alpha = 0.02$. The determined eddy viscosity ν_{eddy} is applied in the region of the expected energy dissipation having length L_b . The duration for the eddy viscosity impact is T_b ; afterwards the wave breaking is assumed to be finished implying $\nu_{eddy} = 0$. The methodology for determining all the required empirical constants is detailed in the work of Tian *et al.* (2012). Further, we designate the given eddy viscosity type of the BEM

TABLE 2. Types of the breaking approximations

Model type	BEMr	BEM ν
Eddy viscosity	$\nu_{eddy} = 0$	$\nu_{eddy} \neq 0$
Regridding	on	off

model as ‘BEM ν ’, see Table 2. In the following part of the paper, we use ‘BEM’ and ‘FNP’ interchangeably when referring to the potential flow model.

2.2. Two-phase Navier-Stokes model (VOF)

A volume-of-fluid (VOF) based two-phase incompressible Navier-Stokes flow solver namely *interFoam*, available in the open source library OpenFOAM, is used in the present work to develop the coupled FNP-NS model. The underlying NS model has been tested extensively for a series of wave-structure interaction problems including dam break, water entry, wave propagation and breaking wave impacting with fixed and moving structures, and the computed results have been verified against analytical solutions, laboratory experiments and other numerical results reported in the literature (Ma *et al.* 2016; Martínez Ferrer *et al.* 2016; Larsen *et al.* 2019). The governing equations of the NS model represent momentum and mass conservation laws supplemented with the transport equation for the volumetric fraction of the water phase:

$$\frac{\partial \rho \mathbf{U}}{\partial t} + \nabla \cdot (\rho \mathbf{U} \mathbf{U}) = \nabla \cdot (\mu \nabla \mathbf{U}) + \sigma \kappa \nabla \alpha - \mathbf{g} \cdot \mathbf{r} \nabla \rho - \mathbf{p}_d \quad (2.7)$$

$$\nabla \cdot \mathbf{U} = 0 \quad (2.8)$$

$$\frac{\partial \beta}{\partial t} + \nabla \cdot (\beta \mathbf{U}) = 0 \quad (2.9)$$

Density of the mixture ρ is determined by using the water volumetric fraction β as follows: $\rho = \beta \rho_w + (1 - \beta) \rho_a$, where ρ_w and ρ_a are the densities of water and air respectively. Similar expression is used to determine the dynamic viscosity of the mixture μ . Equation (2.7) involves the dynamic pressure $\mathbf{p}_d = \mathbf{p} - \rho \mathbf{g} \cdot \mathbf{r}$, where \mathbf{r} is the radius-vector in Cartesian coordinates and \mathbf{g} is the acceleration of gravity. Surface tension is taken into account by the coefficient σ and the local interface curvature κ . The VOF based NS model (2.7)-(2.9) are discretised by a finite volume method on collocated grids and the transient flow problem is solved by the PISO method (Oliveira & Issa 2001). In the following part of the paper, we use ‘VOF’ and ‘NS’ interchangeably when referring to the two-phase incompressible viscous flow model.

To be consistent with the BEM model’s 2D domain, the VOF domain was discretised by cuboid mesh cells with one single layer in the y direction, thus generating a pseudo-2D domain, see Figure 1. The left boundary of the VOF domain was displaced by L_i with respect to the BEM domain as shown in Figure 1. The solution of the BEM model was thus used to determine both the initial and the left boundary condition for the VOF model to establish a one-way coupling between them. The numerical absorption of waves at the end of the domains was performed independently in both BEM and VOF models in order to avoid any interplay between them that may affect the wave train evolution process. The velocity field damping using the effective viscosity was implemented near the far-end boundary of the VOF domain.

TABLE 3. Parameters of the VOF model. Details on the wave trains studied are presented in Section 2.4; λ_0 is the carrier wave length.

	Gaussian wave train	Modulated wave train
Coordinate of the left boundary L_i	3.0 m	30 m
Length of the domain	$24\lambda_0$	$16\lambda_0$
Total height of the domain ($2h$)		1.2 m
Length of the absorbing region		$8\lambda_0$
Grid resolution	256 cells per λ_0	

The Reynolds number for the wave trains considered in the research is (Iafrazi 2009):

$$Re = \frac{\rho_w g^{1/2} \lambda_0^{3/2}}{\mu_w} > 10^5 \quad (2.10)$$

It suggests that non-breaking wave trains may produce turbulence, as demonstrated by Babanin & Chalikov (2012). Even for a two-dimensional problem, the numerical simulation of flows at such high Reynolds number requires enormous computational effort to resolve all the scales involved in wave breaking. Assuming that the nearly laminar flow due to the surface gravity wave is dominant in the problems considered, it is expected to have the grid convergence in terms of free surface elevation. In course of the study it was established that the grid resolution of 256 cells per carrier wave length (λ_0) is sufficient to produce converged solutions while balancing the computational efficiency and the capability to resolve key flow features. The details on the grid independence are given in Appendix A, while the domain configuration is summarised in Table 3.

The spatial and temporal numerical schemes for solution of the equations (2.7) - (2.9) were selected by following the recommendations for the *interFoam* solver (Larsen *et al.* 2019). Adaptive time step was used and the stability criterion was set as $CFL \leq 0.65$.

2.3. Coupling of the FNP and NS models

The coupling of the FNP and NS models was achieved through the following steps. Firstly, the velocity field \mathbf{U} was constructed in the interior area of the BEM domain using the known boundary values of φ and $\partial\varphi/\partial n$. The values of \mathbf{U} in the BEM domain were calculated at the coordinates corresponding to the cell centres of the VOF mesh. Several numerical techniques of evaluation of $\mathbf{U} \equiv \{u, w\} = -\nabla\varphi$ were examined in terms of accuracy and computational efficiency. It was found that the simplest central differencing scheme provides a reasonable accuracy, while keeping the process computationally efficient:

$$\begin{aligned} u &= -\frac{\varphi(x_{cell} + \Delta x, z_{cell}) - \varphi(x_{cell} - \Delta x, z_{cell})}{2\Delta x}, \\ w &= -\frac{\varphi(x_{cell}, z_{cell} + \Delta z) - \varphi(x_{cell}, z_{cell} - \Delta z)}{2\Delta z}, \end{aligned} \quad (2.11)$$

where x_{cell} and z_{cell} are coordinates of the mesh cells of the VOF domain. The resolution of the scheme $\Delta x = \Delta z$ was taken equal to 1/10 of the size of the VOF cell. Other resolutions, i.e. 1/6 and 1/16, were also tested. The values of the potentials $\varphi(x, z)$ in (2.11) were calculated in the BEM solver by selecting the location of the source at the

coordinates $\mathbf{r}_s = (x, z)$ and performing integration of (2.1). Secondly, the BEM velocity field and the free surface profile were used to derive the appropriate boundary and initial conditions for the VOF model.

2.4. Wave train generation

Two types of wave trains are considered in this study. To validate the proposed hybrid BEM-VOF model against the experiments of Tian *et al.* (2012) and Seiffert & Ducrozet (2018), we investigate the wave breaking appearing in a narrow-banded wave train subjected to modulational instability. The surface elevation at the wavemaker location is:

$$\eta(t) = a_0 \cos(\omega_0 t) + b \cos\left(\omega_1 t - \frac{\pi}{4}\right) + b \cos\left(\omega_2 t - \frac{\pi}{4}\right), \quad (2.12)$$

where a_0 and ω_0 are the amplitude and angular frequency of the carrier wave; frequencies of the sideband perturbations are $\omega_1 = \omega_0 - \Delta\omega/2$ and $\omega_2 = \omega_0 + \Delta\omega/2$. The following parameters were adopted from the case MI0719 of Seiffert & Ducrozet (2018) study: $\omega_0 = 4.398 \text{ s}^{-1}$, $\Delta\omega = 0.317$, $b/a_0 = 0.5$. The carrier angular frequency is related to the corresponding wavenumber $k_0(\omega_0)$ by the linear dispersion relation:

$$\omega^2 = \left(gk + \frac{\sigma}{\rho}k^3\right) \tanh(kh), \quad (2.13)$$

For the range of the wavenumbers considered in the paper, capillary effect is not significant so we set $\sigma = 0$. The initial steepness of the wave train was $k_0 a_0 = 0.19$.

A broad-banded Gaussian-shaped focusing wave train was selected for further investigation of the wave breaking phenomenon. This wave train implies the spatial periodicity of the free surface elevation if the domain is sufficiently long, which is critically required for the accurate post-processing of the simulation results. The strongest wave breaking in this case is expected in the vicinity of the focus location whose coordinate relative to the wave generating boundary in the BEM domain ($x = 0$) was selected as $x_f = 8.5 \text{ m}$. The surface elevation variation with time at x_f is:

$$\eta(t, x = x_f) = \zeta_0 \exp\left\{-\left(\frac{t}{mT_0}\right)^2\right\} \cos(\omega_0 t) \quad (2.14)$$

The parameter $m = 0.6$ determines the broad-banded wave train; the carrier wave period and angular frequency are $T_0 = 0.7 \text{ s}$ and $\omega_0 = 2\pi/T_0$, respectively. According to the linear dispersion relation (2.13) the carrier wave length is $\lambda_0 = 2\pi/k_0 = 0.765 \text{ m}$. The dimensionless water depth corresponds to deep water condition (Dean & Dalrymple 1991), i.e. $k_0 h = 4.93 > \pi$. The plot of $\eta(t)$ at the focal point x_f is shown in Figure 3(a); the spatial surface elevation $\eta(x)$ at the instant of focusing t_f is plotted in Figure 3(b).

In this study we investigate the evolution of the free waves, and this requires to exclude the bound waves from the BEM and VOF results. Since bound waves appear predominantly at high and low frequencies with respect to the carrier frequency ω_0 , it is possible to partially avoid their influence by band-pass filtering those regions. Consider the Fourier transform of surface elevation (2.14):

$$\hat{\eta}(\omega) = \mathcal{F}\{\eta(t)\} = \frac{\zeta_0}{2\sqrt{2}} m T_0 \exp\left\{-\pi^2 m^2 \left(1 + \frac{\omega}{\omega_0}\right)^2\right\} \left(1 + \exp\left\{4\pi^2 m^2 \frac{\omega}{\omega_0}\right\}\right) \quad (2.15)$$

The wavenumber spectrum for deep water waves can be obtained by expressing ω from the linear dispersion relation (2.13) and substituting it into (2.15). The energy fraction

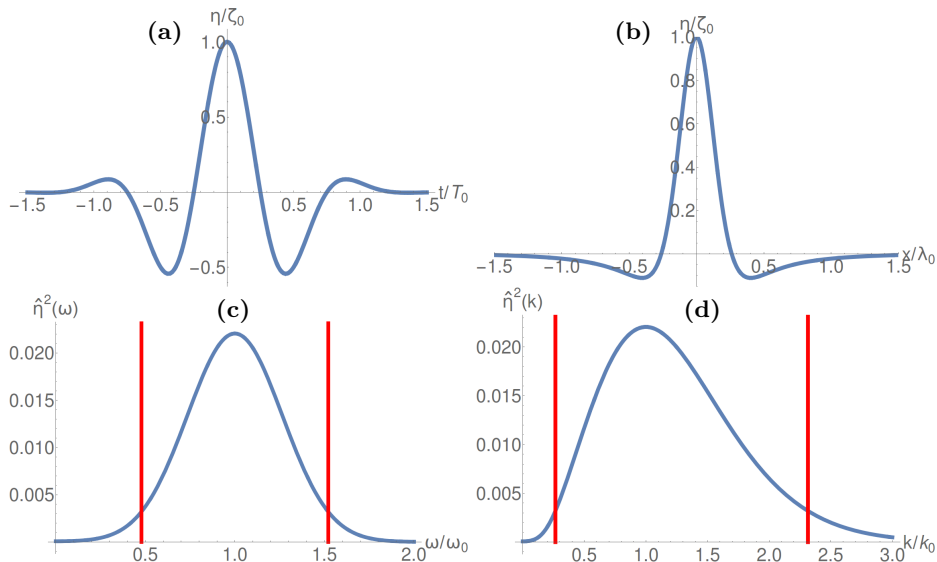


FIGURE 3. Broad-banded Gaussian-shaped focusing wave train considered in the study: (a) free surface elevation at the focal point $x_f = 8.5$ m; (b) wave profile at the focal time $t_f = 0$; (c) frequency and (d) wavenumber power spectra. Vertical red lines designate the range of frequencies and the wavenumbers containing 95% of the spectral energy.

δe contained in the frequency range $[\omega_0 - \Delta\omega, \omega_0 + \Delta\omega]$ is:

$$\delta e = \frac{\int_{\omega_0 - \Delta\omega}^{\omega_0 + \Delta\omega} \hat{\eta}^2 d\omega}{\int_0^{+\infty} \hat{\eta}^2 d\omega} \approx 2\sqrt{2\pi}m \frac{e^{-6\pi^2 m^2} (1 + e^{4\pi^2 m^2})^2}{1 + e^{2\pi^2 m^2}} \frac{\Delta\omega}{\omega_0} \quad (2.16)$$

Solution of (2.16) with respect to $\Delta\omega$ assuming $\delta e = 0.95$ allows to find the frequency band containing 95% of the spectral energy. Following this procedure, the frequency and the wavenumber ranges that will be considered in the further analysis were estimated as follows: $0.48 \leq \omega/\omega_0 \leq 1.52$; $0.27 \leq k/k_0 \leq 2.31$. The power spectra with the corresponding frequency and the wavenumber bounds are depicted in Figures 3 (c) and (d).

Assuming deep water dispersion $k = \omega^2/g$, the spatio-temporal variation of the surface elevation can be obtained from (2.14) and (2.15) by using the linear approximation for water waves:

$$\eta(x, t) = \mathcal{F}^{-1} \{ \hat{\eta}(\omega) \exp [ik(\omega)x] \} = \mathcal{F}^{-1} \left\{ \hat{\eta}(\omega) \exp \left[i \frac{\omega|\omega|}{g} x \right] \right\}, \quad (2.17)$$

where \mathcal{F}^{-1} is the inverse Fourier transform. The linear approximation for the steepness variation in the course of the wave train temporal evolution is:

$$\varepsilon_{max}(t) = \max_{-\infty < x < +\infty} \left| \frac{\partial \eta(x, t)}{\partial x} \right| \quad (2.18)$$

It is known that waves break when their steepness satisfy the condition $\varepsilon > 0.3$. Increasing the wave steepness beyond this value may lead to a single or multiple breaking events. The strength of breaking is also dependent on the value of ε . Varying the value of the constant ζ_0 in (2.14), (2.15) and (2.17), six wave trains of different steepness $k_0\zeta_0 = 0.2, 0.3, 0.4, 0.6, 0.8$ and 1.0 are taken for investigation.

The wave train steepness (2.18) for all considered cases is plotted in Figure 4. As expected for a broad banded focusing wave train, the maximum value of ε_{max} is seen

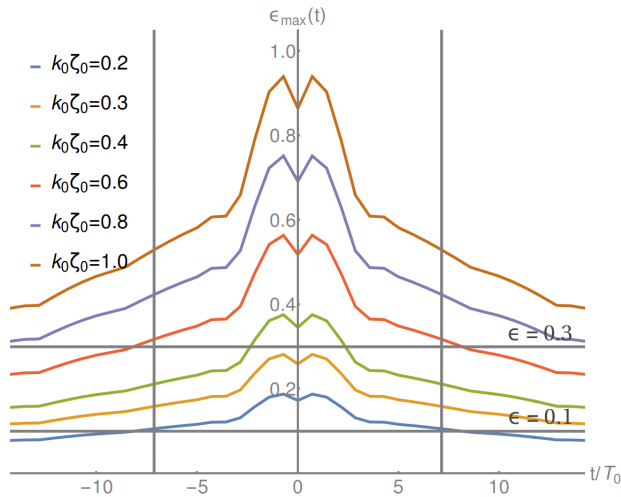


FIGURE 4. Temporal variation of the wave train steepness (2.18) for all considered cases. In this plot, the dispersive focusing appears at $t = 0$. Two gray vertical lines depict the range $-7.14 \leq t/T_0 \leq +7.14$ particularly considered in the study. Within this time interval the full length of the wave train is present in the limits of the computational domain of both BEM and VOF models.

in the vicinity of the focal point, while it reduces farther away from this location. Note that in the course of the study, particular attention is given to the time interval $-7.14 \leq t/T_0 \leq +7.14$, when the full length of the wave train is present within the limits of the computational domain of both BEM and VOF models. The steepness of all wave trains within the given time interval is $\varepsilon_{max} > 0.1$, thus showing the significance of nonlinearities. The mild single breaking event may be expected when $k_0\zeta_0 = 0.3$, because the steepness satisfies the condition $\varepsilon_{max} > 0.3$ near the focal point for this case. If $k_0\zeta_0 \geq 0.6$, the steepness is greater than 0.3 within the entire time interval of interest as shown in the figure. This means that waves may continuously break throughout the evolution of the wave train.

Since the accuracy of wave generation is critical in the current investigation, the 2nd-order accurate method for calculation of the wavemaker motion from the surface elevation was adopted (Khait & Shemer 2019b). The obtained wavemaker motion was then used to control the displacement of the wave-generating boundary in the BEM model, see Figure 1. The surface elevation variation with time at the wavemaker location $\eta(x = 0, t)$ was calculated according to (2.17).

2.5. Spectrum decomposition

It is known that the domains of the free and bound waves may overlap each other in both frequency and wavenumber spectra (Khait & Shemer 2019b). Despite limiting the analysis to a certain frequency range as discussed above, the effect of bound waves on the surface elevation spectrum may still be large leading to complication of the analysis. To facilitate the study, the bound waves should be separated from the free waves by using Zakharov's weakly-nonlinear theory for surface water waves (Zakharov 1968; Stiassnie & Shemer 1984, 1987; Krasitskii 1994). Within this theory, the surface elevation of nonlinear waves may be represented as a series of contributions appearing at different orders of small parameter ε : $\eta = \eta^{(1)} + \eta^{(2)} + O(\varepsilon^3)$; ε is the characteristic wave steepness; $\eta^{(1)}$ and $\eta^{(2)}$ are contributions of the free and the 2nd-order bound waves, respectively.

Application of the Discrete Fourier Transform to the spatial distribution of the free waves surface elevation $\eta^{(1)}$ gives the complex wavenumber spectrum $A(k_m)$, where k_m is the wavenumber of the m -th harmonic. The free wave surface elevation is now:

$$\eta^{(1)}(x) = Re \left\{ \sum_{m=0}^M A(k_m) e^{ik_m x} \right\}, \quad (2.19)$$

where M is the number of the discrete harmonics. Surface elevation of the 2nd-order bound waves is:

$$\eta^{(2)}(x) = Re \left\{ \sum_{m=0}^M \sum_{n=0}^M \left[B(k_m, k_n) e^{i(k_m+k_n)x} + C(k_m, k_n) e^{i(-k_m+k_n)x} + D(k_m, k_n) e^{i(-k_m-k_n)x} \right] \right\}, \quad (2.20)$$

The complex amplitudes $B(k_m, k_n)$, $C(k_m, k_n)$ and $D(k_m, k_n)$ are expressed in terms of $A(k_m)$ as given in Appendix B.

At each instant t , the results of BEM and VOF simulations are processed to determine the distribution of the surface elevation in space $\eta(x)$ as a series of discrete values at 2048 points equidistantly distributed along the domains. The range of the spatial coordinates considered in the analysis is $L_i \leq x \leq L_b$, where L_i corresponds to the inlet boundary of the VOF domain and L_b is the coordinate of the beginning of the absorbing region, see Figure 1. To decompose the fully-nonlinear surface elevation $\eta(x)$ into free and bound waves it is assumed that $\eta(x) \approx \eta^{(1)}(x) + \eta^{(2)}(x)$. From this expression it is possible to find the complex spectra A , B , C and D iteratively by following the algorithm presented in (Shemer *et al.* 2007; Khait & Shemer 2019a). In the first iteration, the free waves spectrum can be taken as $A(k) = \text{FFT}\{\eta(x)\}$, where FFT stands for the Fast Fourier Transform. Usually, 10 to 20 iterations are sufficient to converge the spectrum decomposition. Considering only the separated free waves spectrum $A(k)$ and limiting the analysis to the wavenumbers range found in the preceding section, see Figure 3, it is possible to minimise the effect of bound waves.

3. Model validation and statement of the problem

Breaking in wave trains subject to the modulational instability (2.12) was investigated by Seiffert & Ducrozet (2018). Spatial evolution of waves was tracked in experiments by measuring the surface elevation at several coordinates along the wave flume. In particular, the emphasis was given to the following locations with respect to the wavemaker coordinate ($x = 0$): $x = 30.06$, 34.26 , 37.88 and 50.23 m; the total length of the wave flume is 148 m. They implemented the eddy viscosity approximation proposed by Tian *et al.* (2010, 2012) in a High-Order Spectral (HOS) code. To validate the BEM-VOF numerical model proposed in this paper, we compare our computations with the numerical and experimental results of Seiffert & Ducrozet (2018).

The computed and measured surface elevations are shown in Figures 5 (a)-(d). First, it can be noted that the results of the BEM ν model agree very well with the HOS simulations of Seiffert & Ducrozet (2018). This confirms the validity of the BEM ν model. At the same time, the results of the VOF simulations are very close to the experimental measurements and this demonstrates the accuracy of the two-phase high-fidelity model.

Now compare the results of BEM ν , BEMr and VOF simulations, see Figure 5 (e). It is clearly seen that at a distant location from the wavemaker, $WG14 = 50.23$ m, the plots of BEM ν and BEMr computations are close to each other. This suggests that

the simple remeshing technique implemented in the BEMr model (Subramanya & Grilli 1994) can produce as good results as the complicated eddy viscosity approximation. It can be clearly seen that there is a significant discrepancy between the low-fidelity calculations and the experiment from about 62.5 to 64.5 seconds regarding the peak elevations, potentially critical to maritime safety. While the high-fidelity results are quite close to the measurements in terms of peak surface elevation. Similar observations were reported by Tian *et al.* (2012) and Seiffert & Ducrozet (2018). Seiffert & Ducrozet (2018) attempted to address this issue by modifying the eddy viscosity approximation without receiving much success.

The eddy viscosity approximation for wave breaking is based on the weakly-damped wave theory (Ruvinsky *et al.* 1991; Dias *et al.* 2008), which assumes the rotational components of the fluid velocity to be small. However, strongly breaking waves may generate significant non-potential flows; such as sheared currents, vortices, etc. (Iafrati *et al.* 2013; Deike *et al.* 2017; Lenain *et al.* 2019). This could be a reason for the eddy viscosity method producing inaccurate prediction of surface elevation.

4. Results and Discussion

4.1. Surface elevation

Here we investigate the evolution of Gaussian-shaped broad-banded wave trains (2.14) by using the standalone FNP model and the hybrid FNP-NS model. We selected a series of representative wave trains with steepness of $k_0\zeta_0 = 0.2, 0.3, 0.4, 0.6, 0.8$ and 1. Computed surface elevations recorded at $x = 4.5$ m, $x = x_f = 8.5$ m (x_f is the expected focal point), and $x = 12.5$ m are plotted in Figure 6. For wave trains with low steepness $k_0\zeta_0 \leq 0.4$, there is only one mild breaking event or even no breaking at all. Thus the eddy viscosity closure was not used for the cases illustrated in the panels (a)-(c).

Figure 6(a) shows perfect coincidence of the results obtained by BEMr and VOF simulations when no breaking is present. It confirms the effectiveness of the BEM-VOF coupling used in the current study. The shape of the wave train at the focal point $x_f = 8.5$ m is very close to the linear prediction shown in Figure 3(a). However, since the wave train is substantially nonlinear, a certain amount of asymmetry of the surface elevation before and after the focal point can be noticed. An increase in steepness, i.e. Figures 6(b) and (c), leads to a significant deviation of either the BEMr solution or the VOF result from the linear estimation at the focal point, as expected for the steeper nonlinear waves. For the cases with higher steepness parameter $k_0\zeta_0 \geq 0.6$ shown in Figure 6 (d)-(f), both the BEMr and BEM ν models were used. In compliance with the previous results, see Section 3, no significant difference was noticed between the BEMr and BEM ν results. Therefore, further analysis in the paper will be based on the BEM ν model.

For wave trains with strong breaking shown in Figure 6 (d)-(f), the BEM ν and VOF models produced quite similar results at $x = 4.5$ m. On the contrary, in the vicinity and beyond the focal point, a considerable deviation between BEM ν and VOF results is found and it increases with the steepness $k_0\zeta_0$. This indicates that certain physical processes associated with the breaking events are not accurately reflected by the quasi-potential eddy viscosity approximation in BEM ν . It seems that this phenomenon is similar to the discrepancy we observed in Section 3 for the experiments of Tian *et al.* (2012) and Seiffert & Ducrozet (2018).

Flooding contours of the velocity magnitude underneath the free surface are plotted in Figure 7 so that we can have a close look at the flow field to study the difference between the two-phase VOF solutions and the fully-nonlinear potential BEM ν results.

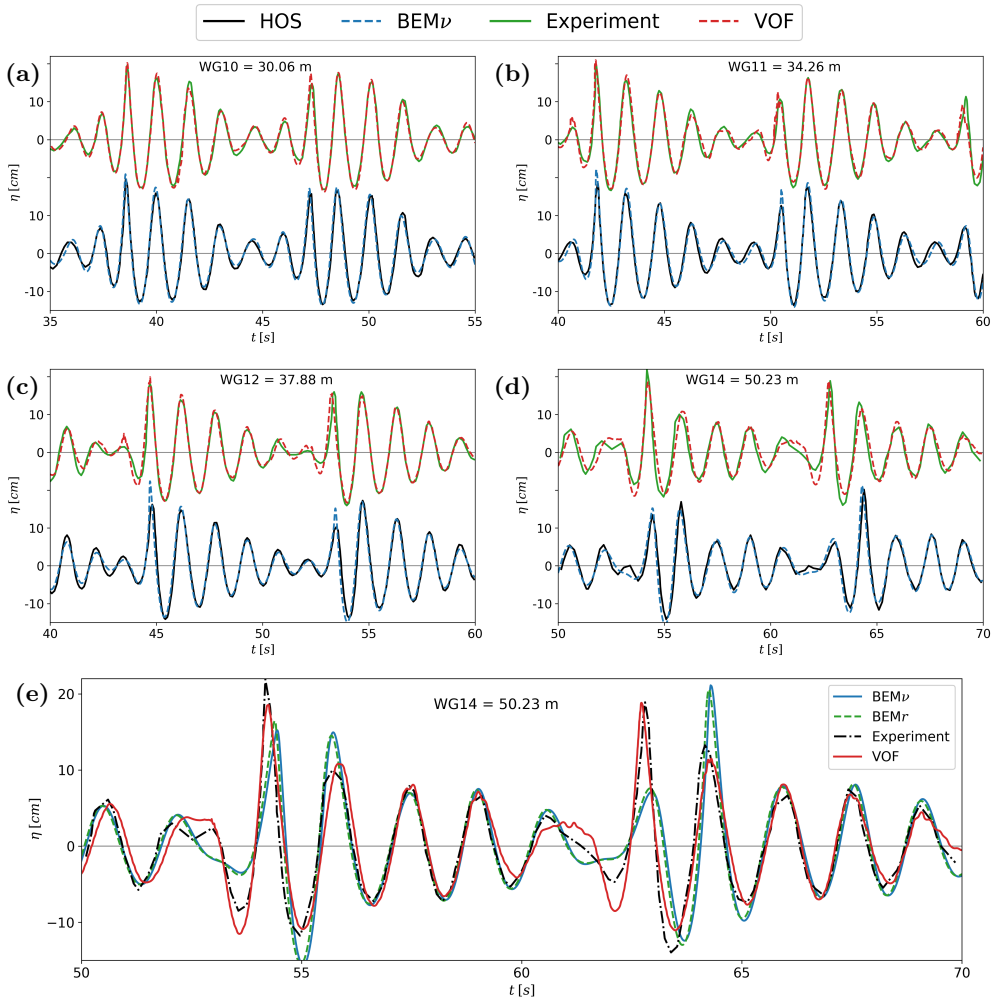


FIGURE 5. Measured and calculated surface elevations for a wave train subject to modulational instability at four wave gauges: WG10 = 30.06 m, WG11 = 34.26 m, WG12 = 37.88 m and WG14 = 50.23 m. Solid black line: high order spectral simulations of Seiffert & Ducrozet (2018); Solid green line: experiments of Seiffert & Ducrozet (2018); Blue dashed line: solution of the present FNP model with the eddy viscosity enclosure; Red dashed line: result of the present NS model.

The fields are derived at $t = 35$ s near $x_f = 8.5$ m corresponding to the temporal and spatial location of the expected focal point according to the linear wave dispersion. The $BEM\nu$ model shows a quite smooth distribution of the velocity in the domain, contrary to the VOF solution, which embraces a certain perturbation component due to the vortical part of the flow. The plots show that the amplitude of the vortical velocity $-\nabla \times \Psi$ is no longer small as assumed in the weakly-damped theory used by Tian *et al.* (2010, 2012). Consequently, the applicability of the eddy viscosity model for these problems is in question.

It is expected that the vortical flow consists of the sheared currents and other local and distributed non-potential fluid motions (Iafrafi *et al.* 2013; Deike *et al.* 2017; Lenain *et al.* 2019). For instance, several vortical structures are clearly shown in Figures 7 (b) and (c).

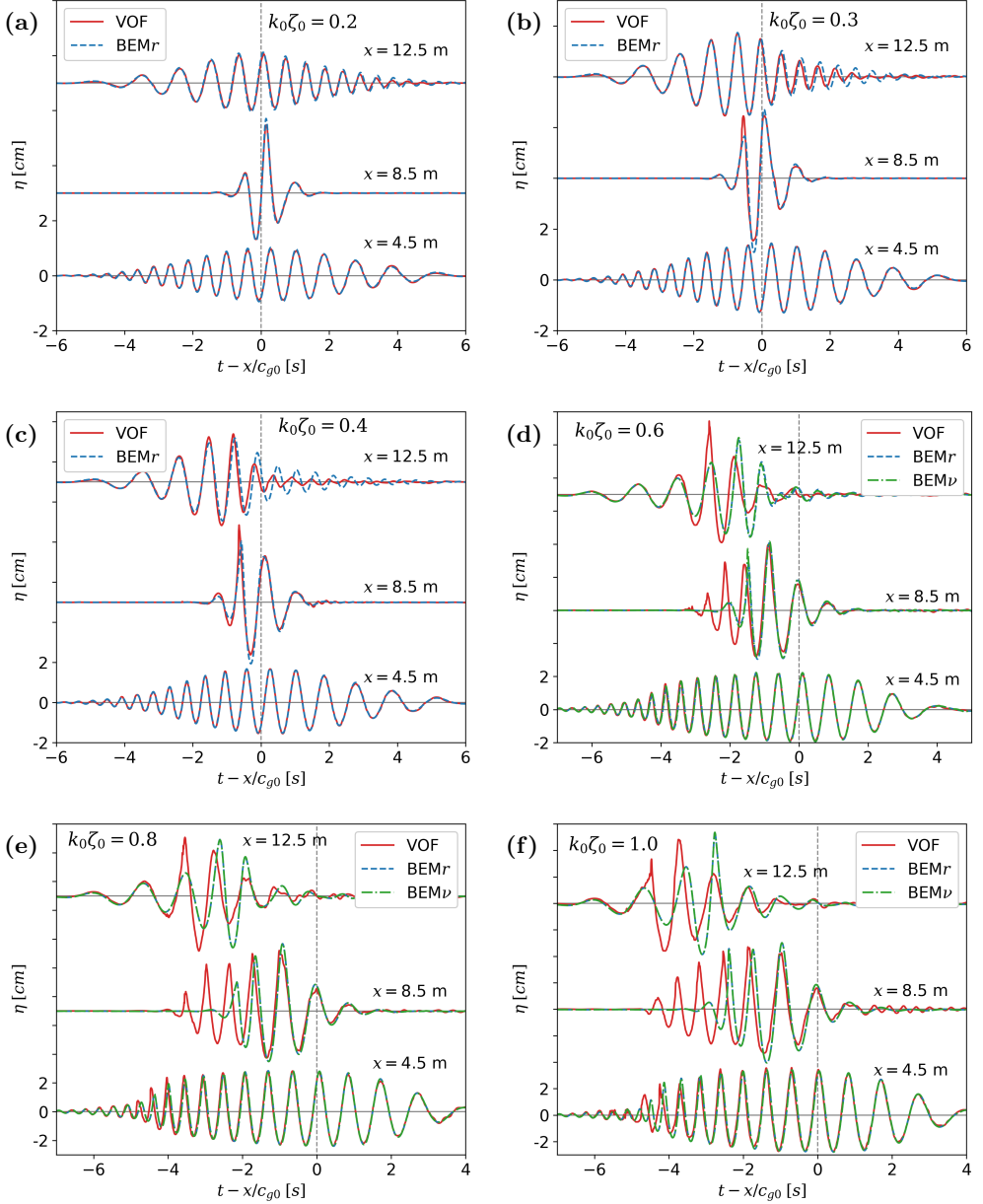


FIGURE 6. Surface elevation variation with time obtained by three numerical models: VOF, BEMr and BEM ν . The value of time in the horizontal axes was displaced using the group velocity c_{g0} calculated for the carrier (peak) frequency of the wave train spectrum. The linear dispersive focusing is expected at $t - x/c_{g0} = 0$.

A more detailed investigation of the non-potential flows supposes the need of quantitative comparison of the BEM ν and VOF velocity fields. But a meaningful comparison is practically impossible for the considered cases because the shapes of free surface obtained by these models are very different.

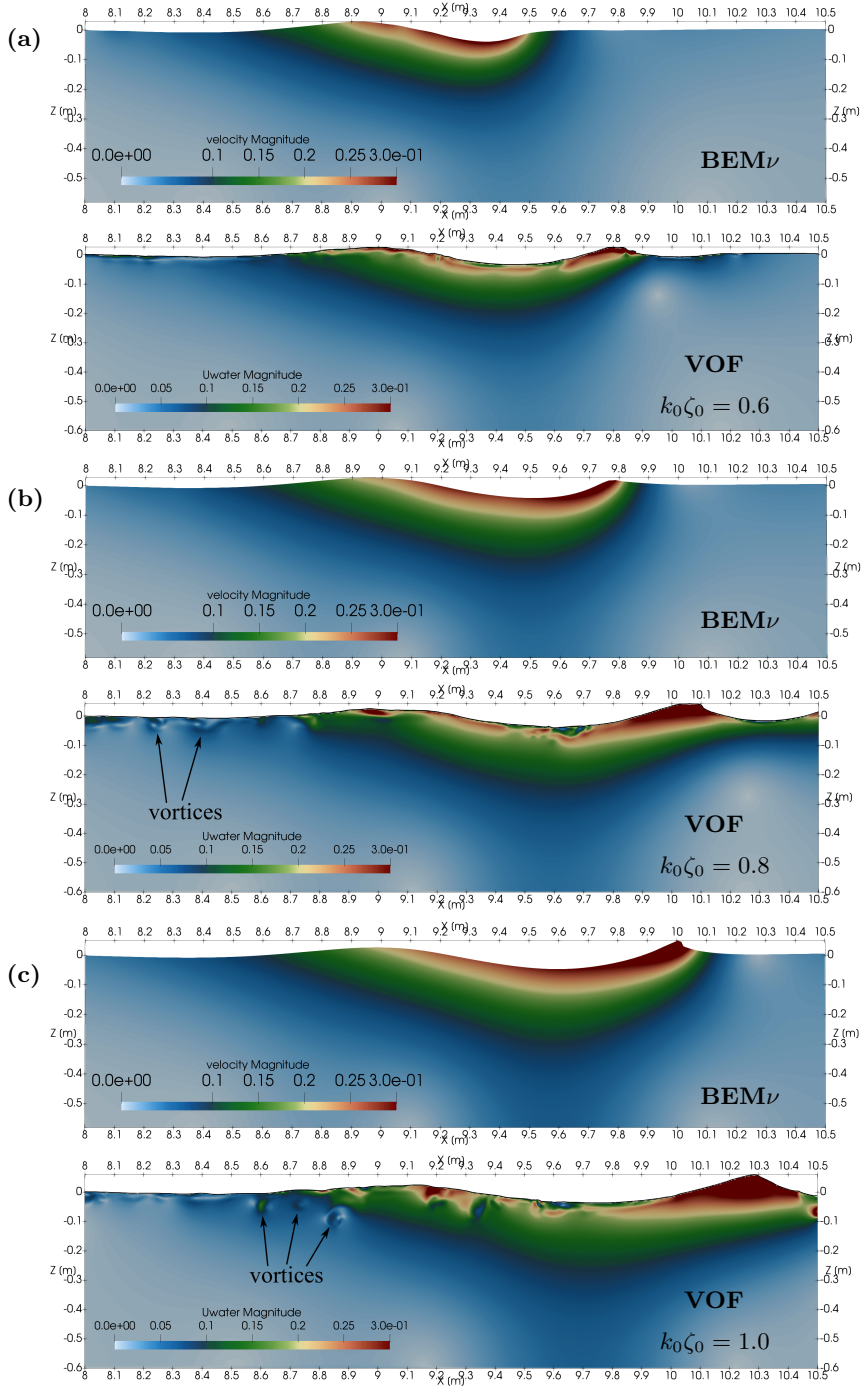


FIGURE 7. Distribution of the velocity magnitude $|\mathbf{U}|$ beneath the free surface obtained in the BEM ν and VOF models for three strongly breaking cases: (a) $k_0\zeta_0 = 0.6$, (b) $k_0\zeta_0 = 0.8$, and (c) $k_0\zeta_0 = 1.0$. The plots are obtained at the instant of focusing $t_f = 35$ s and in the vicinity of the focal point $x_f = 8.5$ m: the horizontal scale is $8 \leq x \leq 10.5$ m.

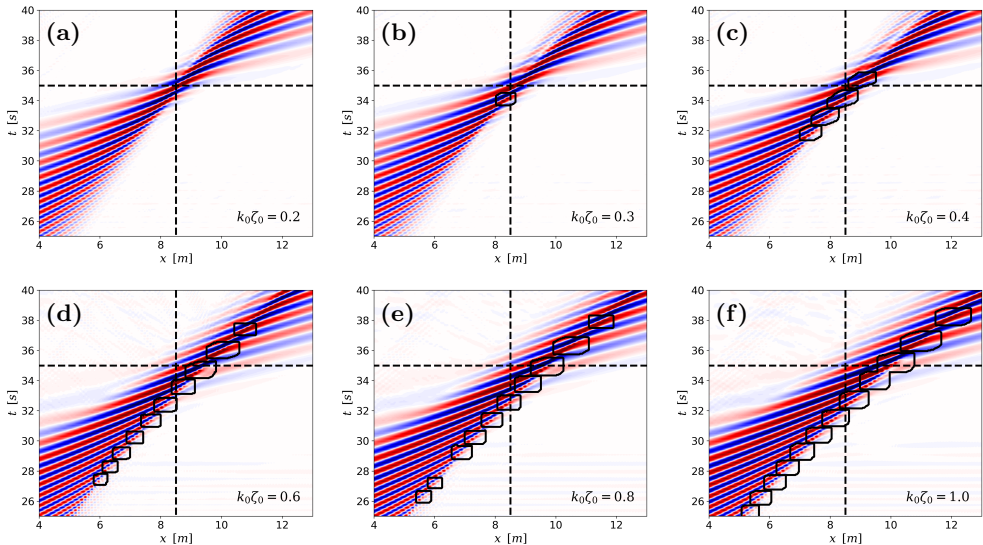


FIGURE 8. Energy dissipation regions predicted by the eddy viscosity approximation. Panels (a)-(f) present the wave trains having steepness parameter $k_0\zeta_0 = 0.2, 0.3, 0.4, 0.6, 0.8,$ and 1.0 , respectively. The breaking regions are depicted by black solid lines. Color shows the spatio-temporal variation of the surface elevation $\eta(x, t)$ calculated by the BEM ν model. Dashed lines show the location of the focal point expected according to the linear dispersion.

4.2. Energy dissipation due to wave breaking

The spatio-temporal evolution of the wave train calculated by the BEM ν model is illustrated in Figure 8 in terms of surface elevation. Wave breaking regions are highlighted in the figure as rectangular areas enclosed by black solid lines. The dimensions of these regions L_b in space and T_b in time were determined by the eddy viscosity closure (2.6). For each region the constant value of the eddy viscosity ν_{eddy} was calculated by using the formula (2.5). As expected, the non-breaking case, i.e. Figure 8(a), does not have any predicted breaking locations. We also note that increasing the steepness $k_0\zeta_0$ can cause multiple breaking events instead of a single very strong one. This is because the wave train loses its stability much ahead of the focal point. At the same time, larger values of ν_{eddy} correspond to more energy dissipation.

The energy dissipation locations shown in Figure 8 do not overlap with each other. This means that in the studied wave trains, waves always break at different locations. Before the focal point, breaking always appears at the leading edge of the wave train because of the presence of short steep waves. On the contrary, after the focal point breaking locations move closer to the centre of wave train. Taking into account the fact that the leading edge of the wave train after the focal point consists of long waves, it can be assumed that those waves are more stable. This observation is usually involved in the spectral models of water waves, where the energy dissipation mostly at high frequencies is incorporated (Babanin *et al.* 2011; Annenkov & Shrira 2018).

Within the eddy viscosity quasi-potential approach, the energy dissipation process can be seen as a transformation of the nonlinear surface wave energy into the rotational fluid flow energy. Since the considered broad-banded wave train occupies a restricted space, it is convenient to estimate the strength of the wave breaking by tracing the amount of energy transferred by the wave train through different cross sections, i.e. integral energy

flux (Banner & Peirson 2007; Drazen *et al.* 2008; Tian *et al.* 2008; Derakhti & Kirby 2016). Taking into account that wave breaking is a strongly localised phenomenon, the energy loss is associated with a particular location and appears as a reduction of the integral energy flux across the breaking location.

The total integral energy flux passing through the cross section x in the VOF model is given by:

$$F_{VOF}^{NL}(x) = \int_{-\infty}^{+\infty} dt \int_{-h}^{+h} \left\{ \frac{1}{2} \rho_w |\mathbf{U}|^2 + \rho_w g z + p \right\} u \beta dz, \quad (4.1)$$

where $\mathbf{U} = (u, w)$. This expression does not involve any physical simplification and thus determines the fully-nonlinear (NL) value of the energy flux. In the VOF model, the volume fraction β is used to determine the percentage of water contained in a mesh cell. Thus the height of the water layer in each cell is βdz . The so-called dry and wet cells are distinguished by $\beta = 0$ and $\beta = 1$, respectively. Determination of the nonlinear energy flux in the BEM ν model is more complicated because the needed pressure p is not readily available in the solution. Simplification of (4.1) can be achieved by using the Bernoulli equation (2.3) and taking $\mathbf{U} = -\nabla\varphi$:

$$F_{BEM}^{NL}(x) = -\rho_w \int_{-\infty}^{+\infty} dt \int_{-h}^{\eta(x,t)} \frac{\partial\varphi}{\partial t} \frac{\partial\varphi}{\partial x} dz \quad (4.2)$$

In laboratory it is not feasible yet to measure the nonlinear energy flux. Instead, a linearisation of (4.2) is usually applied (Banner & Peirson 2007; Drazen *et al.* 2008; Tian *et al.* 2008; Derakhti & Kirby 2016; Tian *et al.* 2010, 2012; Seiffert & Ducrozet 2018). Researchers usually assume the equipartition of total energy between the kinetic and potential parts, which is admissible for linear wave system. The linear approximation for the total energy density is $E = \rho_w g \overline{\eta^2}$, where the overbar represents averaging over the local wavelength. The linear approximation for the energy flux is then given by (Dean & Dalrymple 1991; Drazen *et al.* 2008; Derakhti & Kirby 2016):

$$F^L(x) = \int_{-\infty}^{+\infty} E c_{gs} dt = \int_{-\infty}^{+\infty} \rho_w g c_{gs} \eta^2 dt \quad (4.3)$$

Here c_{gs} is the spectral-weighted group speed approximating the velocity of energy transferred by the given wave train:

$$c_{gs} = \frac{\sum_j c_{g,j} a_j^2}{\sum_j a_j^2}, \quad (4.4)$$

where a_j and $c_{g,j}$ are the amplitude and the group velocity of the j^{th} component of the wave packet spectrum.

The outcomes of (4.1) and (4.3) are compared in Figure 9 for the steepest wave train with $k_0 \zeta_0 = 1.0$. The dimensionless variables are introduced: energy flux $\hat{F} = F/F_0$ and spatial coordinate $\hat{x} = x/\lambda_0$; F_0 is the initial energy flux computed at $x \approx 0$. Figure 9 shows that the distributions of linear energy flux computed by the BEM ν and VOF models, i.e. $F_{BEM\nu}^L$ and F_{VOF}^L , somewhat deviate from each other. The nonlinear energy flux F_{VOF}^{NL} obtained by the VOF model provides the highest values of \hat{F} . In spite of slightly different trajectories, the values of $F_{BEM\nu}^L$, F_{VOF}^L and F_{VOF}^{NL} at the outlet of the domain, i.e. behind the active breaking region, are quite close to each other. This suggests that the eddy viscosity approximation used in the BEM ν model predicts quite accurately the energy dissipation process, in agreement with earlier investigations (Tian *et al.* 2010, 2012; Seiffert & Ducrozet 2018; Hasan *et al.* 2019). It is interesting to note that the

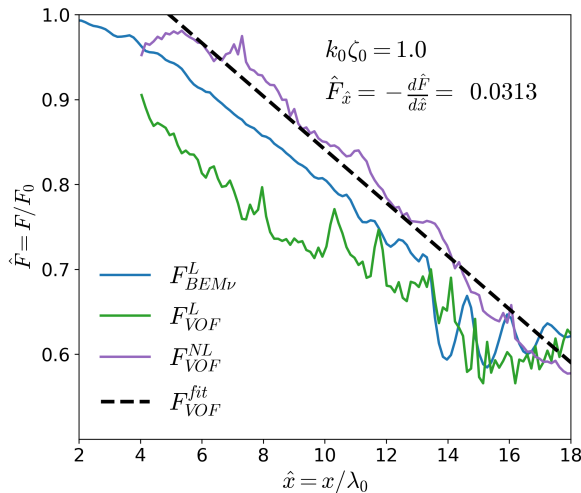


FIGURE 9. Distribution of the dimensionless integral energy flux $\hat{F} = F/F_0$ along the computational domain $\hat{x} = x/\lambda_0$ for the wave train with the steepness parameter $k_0\zeta_0 = 1.0$.

TABLE 4. The values of the energy dissipation rate computed for the wave trains of different steepness.

$k_0\zeta_0$	$\hat{F}_{\hat{x}} = -d\hat{F}/d\hat{x}$
0.3	0.00695
0.4	0.00852
0.6	0.0196
0.8	0.0284
1.0	0.0313

discrepancy in surface elevation calculation (see Figure 6) doesn't significantly affect the amount of wave energy dissipated by breaking.

In the present work, we use the mean gradient of nonlinear energy flux $\hat{F}_{\hat{x}} = -d\hat{F}/d\hat{x}$ to characterise the strength of breaking. Such a quantify can be interpreted as the wave energy dissipation rate in space. For the VOF model, we produced the best fit of the energy flux F_{VOF}^{fit} and illustrated it in Figure 9 as the black dashed line, which has a gradient of 0.0313 in magnitude. The distributions of F_{VOF}^{NL} and F_{VOF}^{fit} for wave trains with different steepness $k_0\zeta_0$ are plotted in Figure 10. The calculated values of $\hat{F}_{\hat{x}}$ are summarised in Table 4. It can be seen from Figure 10 and Table 4 that the energy dissipation rate $\hat{F}_{\hat{x}}$ increases with the wave train steepness $k_0\zeta_0$.

4.3. Shift of phase due to wave breaking

In the beginning and at the end of computations only a part of the wave train is present within the domain. Therefore, in the analysis we focus on the interval $30 \leq t/T_0 \leq 56.8$, when the full length of the wave train is present within the domain. The surface elevation of free waves (2.19) obtained by the spectral decomposition (see Section 2.5) of simulation

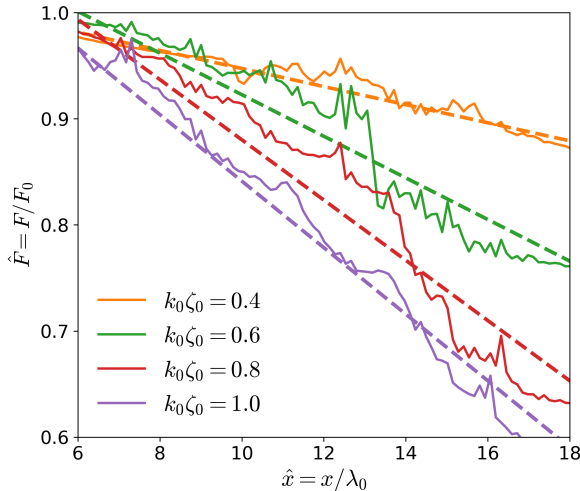


FIGURE 10. Distribution of the nonlinear energy flux F_{VOF}^{NL} obtained by the VOF model. The solid curves correspond to energy fluxes produced by the wave trains of different steepness $k_0\zeta_0$. The dashed lines show the best fit of the data needed to compute the energy dissipation rate $\hat{F}_{\hat{x}}$.

results can be written as:

$$\eta^{(1)}(x) = \sum_{m=0}^M |A(k_m)| \cos(k_m x + \xi_m), \quad (4.5)$$

where the phase is given by:

$$\xi_m = \tan^{-1} \frac{\text{Im}\{A(k_m)\}}{\text{Re}\{A(k_m)\}}. \quad (4.6)$$

It was found that the amplitude spectra obtained from the BEM ν and VOF simulations are practically identical in terms of the absolute value of the amplitude $|A(k_m, \omega_m)|$ regardless of wavenumber and angular frequency, cf. Figure 11 (a)-(d). This observation confirms the capability of the eddy viscosity approximation in predicting wave energy dissipation, which is in line with previous studies (Tian *et al.* 2010, 2012; Seiffert & Ducrozet 2018; Hasan *et al.* 2019), see also Figure 9. Note that the energy contained in the spectrum is $\sum_{m=0}^M |A(k_m, \omega_m)|^2$. Therefore the visible divergence in surface elevation shown in Figure 6 is very likely caused by the phase ξ_m . The phase difference between the VOF and BEM ν results relative to the carrier wave characteristics $\omega_0 T_0$ is given by:

$$\frac{\Delta \xi_m}{\omega_0 T_0} = \frac{1}{2\pi} (\xi_{m,\text{VOF}} - \xi_{m,\text{BEM}\nu}) \quad (4.7)$$

The evolution of $\Delta \xi_m$ in time for different wavenumber k_m is plotted in Figure 12 for the wave trains with steepness $k_0\zeta_0 \geq 0.4$.

Figure 12 reveals a quite smooth and deterministic rather than stochastic evolution of the phase shift $\Delta \xi$ in time. Moreover, there is a strong dependence of $\Delta \xi$ on the wavenumber. The phase shift is relatively small at low wavenumbers, while at a high wavenumber it has a much pronounced growth with time. For instance, at the end of the wave breaking region the phase shift for a high wavenumber $k/k_0 \approx 1.5$ can increase by more than one full revolution, see Figure 12(d). If the wave train steepness $k_0\zeta_0$

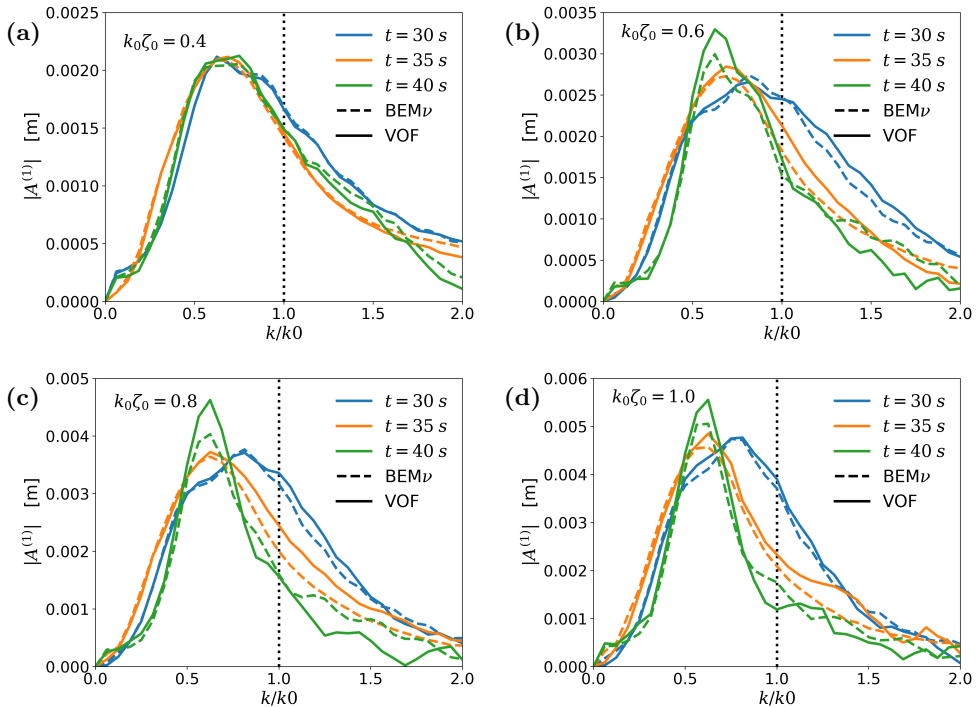


FIGURE 11. Free wave spectra obtained in VOF (solid lines) and BEM ν (dashed lines) models. Panels (a)-(d) present the wave trains of different steepness parameter $k_0\zeta_0$. Plots of different colour are obtained at various times of simulations.

and subsequently the energy dissipation rate $\hat{F}_{\hat{x}}$ are relatively low, the corresponding phase shift is much weaker, see Figure 12(a). The phase difference between the BEM ν and VOF calculations could be due to the fact that the highly nonlinear rotational flows generated by breaking cannot be properly handled by the weakly-potential eddy viscosity approximation.

Considering the dependence of phase shift on the wavenumber k and time t for the breaking strength $\hat{F}_{\hat{x}}$, we approximate it with the following expression:

$$\frac{\Delta\xi}{\omega_0 T_0} \Big|_{\hat{F}_{\hat{x}}} = \Xi \left[\frac{k}{k_0} \right]^{\Theta_K} \left[\frac{t}{T_0} \right]^{\Theta_T} \quad (4.8)$$

The values of three coefficients Ξ , Θ_K and Θ_T change from one wave train to another due to different breaking strength. We applied the least squares method to obtain the dependencies $\Xi(\hat{F}_{\hat{x}})$, $\Theta_K(\hat{F}_{\hat{x}})$, and $\Theta_T(\hat{F}_{\hat{x}})$ from the numerical simulations, and present them in Figure 13. It is shown that the rate of phase shift has a nonlinear dependence on time and wavenumber for relatively weak breaking; i.e. the values of the power coefficients $\Theta_K \approx \Theta_T \approx 4$ when $\hat{F}_{\hat{x}} < 0.01$. If breaking is strong, the dependence of the phase shift on time tends to be linear with $\Theta_T \approx 1$, while the dependence on wavenumber is close to quadratic with $\Theta_K \approx 2$. Both Θ_K and Θ_T are reduced almost linearly with the increase of breaking strength $\hat{F}_{\hat{x}}$. In turn, the proportionality coefficient $\Xi(\hat{F}_{\hat{x}})$ demonstrates an exponential dependence on the energy dissipation rate $\hat{F}_{\hat{x}}$. Therefore it seems reasonable to infer from the analysis that the phase shift can become quite significant for strong breaking events.

We applied the similar interpolation function to all the considered wave trains and

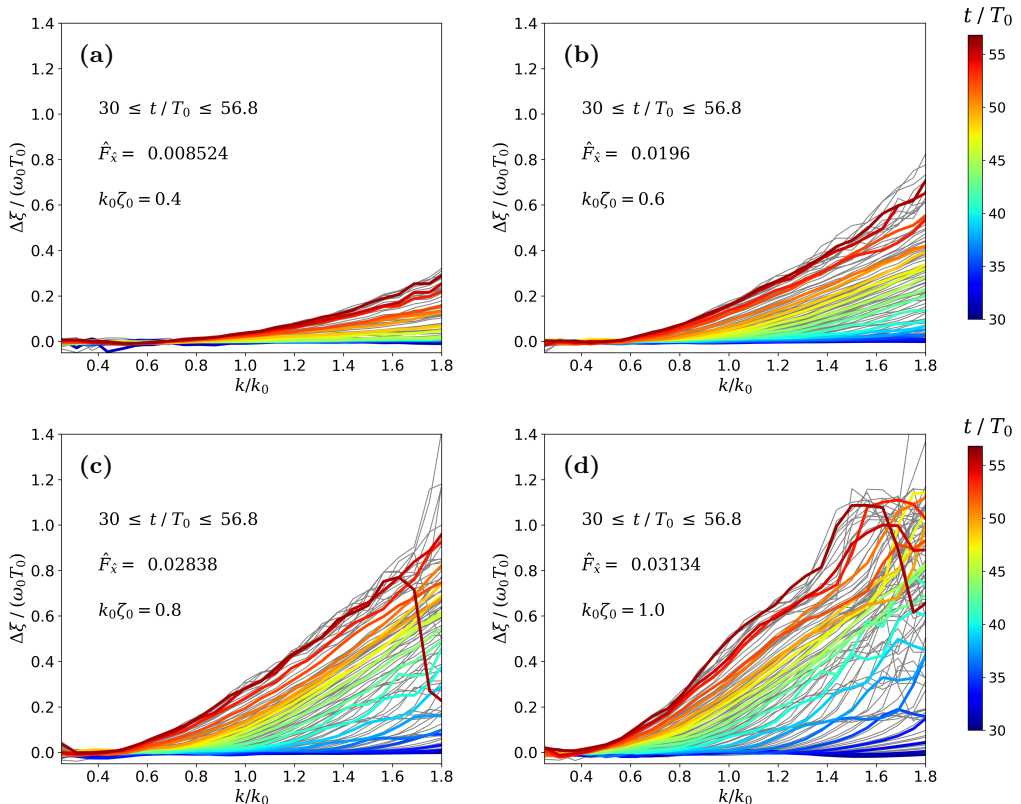


FIGURE 12. Evolution of difference in the free waves phases $\Delta\xi_m$ between VOF and BEM simulations. The color scheme from blue to red displays the plots obtained at different instances within the range $30 \leq t/T_0 \leq 56.8$. Gray plots show other not colored data within the same time interval. Panels (a)-(d) correspond to the wave trains of various steepness $k_0\zeta_0$.

TABLE 5. Values of the dimensionless coefficients in the expression (4.9)

Ξ	Θ_F	Θ_K	Θ_T
5.02	1.926	2.362	1.2105

obtained the corresponding phase shift in a dimensionless form:

$$\frac{\Delta\xi}{\omega_0 T_0} = \Xi \left[\hat{F}_x \right]^{\Theta_F} \left[\frac{k}{k_0} \right]^{\Theta_K} \left[\frac{t}{T_0} \right]^{\Theta_T} \quad (4.9)$$

Applying the least squares fitting of the numerical results, we obtained the coefficients and listed them in Table 5. In addition to the previous findings, the value of $\Theta_F \approx 2$ implies a quadratic dependence of the phase shift on the energy dissipation rate.

In Figure 14 the raw plots of $\Delta\xi(k, t)$ obtained from the numerical simulations are compared with those reconstructed from (4.9) in order to study the accuracy of the suggested approximation. It can be noticed that the plots obtained directly from the

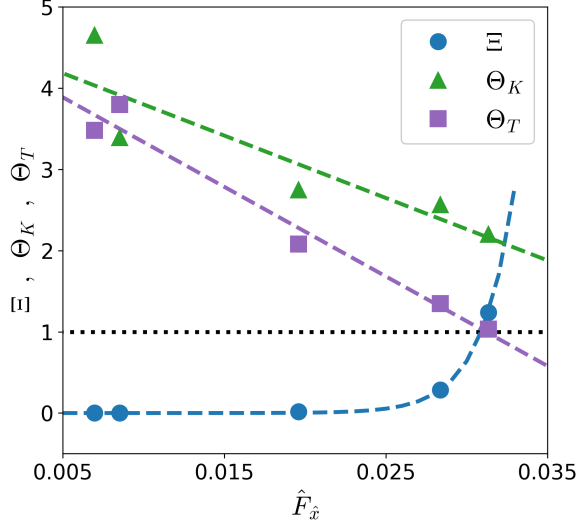


FIGURE 13. Dependence of the fitting coefficients Ξ , Θ_K and Θ_T (4.8) on the wave breaking strength $\hat{F}_{\hat{x}}$.

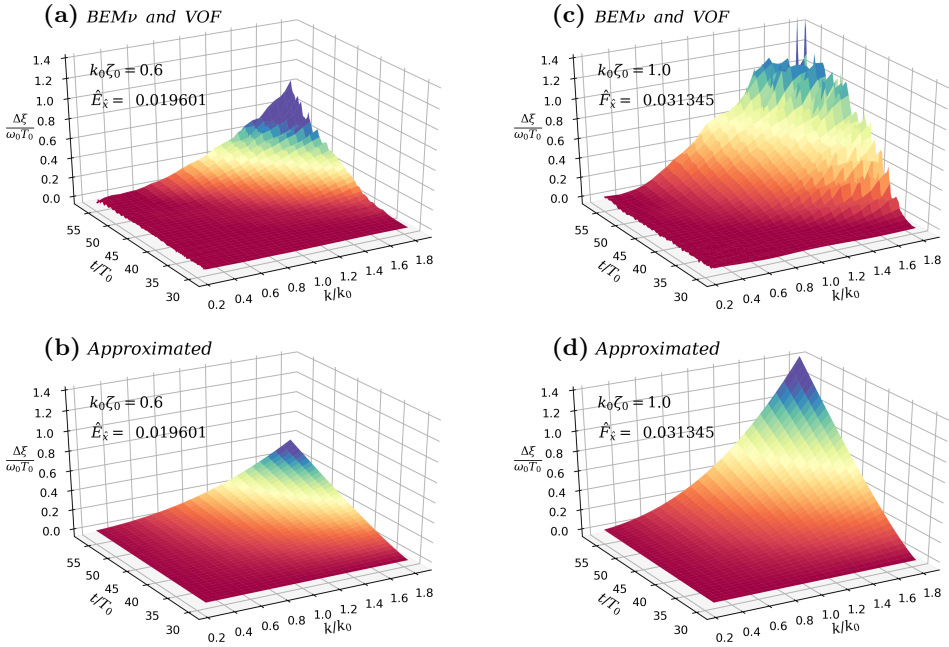


FIGURE 14. Phase shift $\Delta\xi/\omega_0 T_0$ as a function of wave number and time obtained for the wave trains of different breaking strength: (a) and (b) $\hat{F}_{\hat{x}} = 0.0196$; (c) and (d) $\hat{F}_{\hat{x}} = 0.0313$. Panels (a) and (c) present the raw phase shift calculated using (4.7), while panels (b) and (d) are plotted using the interpolation (4.9).

simulations using (4.7), see panels (a) and (c), exhibit fluctuations at high wavenumbers because the bound waves are not perfectly separated from the free waves by the decomposition method (section 2.5). Even minor presence of unseparated bound waves significantly influences phases of the harmonics. Function (4.9) filters the fluctuations from the plots as presented in panels (b) and (d), while keeping a good qualitative and quantitative correspondence with the raw data extracted from the simulations.

The observed shift in phase is possibly related to the so-called phase-locking phenomenon reported by Derakhti & Kirby (2016). The phase-locking processes is considered as a nonlinear linkage between high- and low-frequency wave components. This linkage was demonstrated by analysing the wavelet spectra of the surface elevation in the vicinity of the breaking event (Derakhti & Kirby 2016). The propagation velocity of the high frequency components of the breaking wave was found to be different from that of the pre-breaking but stable wave.

4.4. Dispersion variation

It has been shown in various studies that the relationship between wavenumber and frequency may deviate from the linear dispersion relation (2.13) when the frequency spectrum is narrow. Krogstad & Trulsen (2010) studied the dynamic nonlinear evolution of unidirectional Gaussian wave packets using the nonlinear Schrödinger equation and its generalisations. It was observed that in the k - ω space the spectrum does not maintain a thin well-defined dispersion surface but develops into continuous distribution. The spectral components above and below the spectral peak were found to have the phase and group velocities close to that of the spectral peak. It was concluded that in some cases it is inappropriate to use the linear dispersion relation for the post-processing of experimental data.

Houtani *et al.* (2018*a,b*) have demonstrated that the dispersion characteristics of the Akhmediev breather solution to the nonlinear Schrödinger equation in deep water deviates significantly from the linear relationship (2.13). It was also shown that these findings extend beyond the applicability of nonlinear Schrödinger equation. Accordingly, the highly nonlinear non-breaking modulated wave trains also maintain the straight line relationship between the wavenumber and the instantaneous frequency; this line is tangent to the dispersion relation curve (2.13) at the carrier wavenumber. Gibson & Swan (2006) investigated the waves dispersion using the numerical simulations based on the 3rd-order Zakharov equation. Inconsistency of the simulation results with the linear wave dispersion (2.13) was explained by analysing the third-order resonant interactions. The nonlinear energy transfer between harmonics in the free wave spectrum alters the values of the complex amplitudes. If interacting wave components are out of phase, this energy transfer will change the instantaneous phases of waves, which is reflected in the k - ω space. Adopting a similar Zakharov equation based theoretical model, the nonlinear correction to the dispersion relation for gravity waves in a constant depth was derived analytically by Stuhlmeier & Stiassnie (2019).

The phase of each free wave component is (Houtani *et al.* 2018*b,a*):

$$\xi(k, \omega, t) = kx - \omega t - \delta^{NL}(k, t), \quad (4.10)$$

where $\delta^{NL}(k, t)$ is the slowly varying nonlinear phase induced by the 3rd-order resonant interaction between the waves (Gibson & Swan 2006). The angular frequency can be found from (4.10) by involving (2.13):

$$\omega(k) = -\frac{\partial \xi(k, \omega, t)}{\partial t} = \sqrt{gk \tanh(kh)} + \left\langle \frac{\partial \delta^{NL}(k, t)}{\partial t} \right\rangle \quad (4.11)$$

When analysing a long time evolution of the wave group, the influence of $\langle \partial \delta^{NL} / \partial t \rangle \neq 0$ seen in k - ω spectrum may be interpreted as a deviation of the relationship $\omega(k)$ from (2.13).

In the current study it was found that the nonlinear contribution $\delta^{NL}(k, t)$ can be caused by the resonant interactions as well as the breaking-induced rotational flows. To construct the k - ω spectrum from BEM ν and VOF computations the discrete distribution of the surface elevation in space is extracted from the numerical results. After applying spectrum decomposition (see Section 2.5) the elevations of free waves at different instants are expressed as a function $\eta(x, t)$. The discrete 2D Fourier transform of this function in the k - ω space is given by:

$$\hat{\eta}(k, \omega) = \frac{1}{NM} \sum_x \sum_t \eta(x, t) e^{i(kx - \omega t)}, \quad (4.12)$$

where N and M are the number of discrete values of η in x and t directions, respectively. Distributions of the absolute values $|\hat{\eta}(k, \omega)|$ obtained from the VOF simulations are shown in Figure 15.

The highest values of $|\hat{\eta}(k, \omega)|$ are located in a relatively narrow region approximately defining the dispersion relation $\omega(k)$. For the considered broad-banded Gaussian wave trains the distributions of $|\hat{\eta}(k, \omega)|$ have no visible deviation from the linear dispersion relation for both non-breaking and weakly-breaking cases $k_0 \zeta_0 = 0.3 - 0.4$, cf. Figure 15 (a) and (b). According to Figure 4, the maximum steepness of these wave trains is within the interval $0.2 < \varepsilon_{max} < 0.4$, indicating strong non-linearity. Such dispersive properties are different from those discussed in (Gibson & Swan 2006; Krogstad & Trulsen 2010; Houtani *et al.* 2018*b, a*), where the linear dispersion relation was found to be inaccurate. The difference in the wave packet evolution may be related to the width of the spectra that is significantly higher for the wave trains considered in the current study.

Subsequent increase of the wave train steepness, i.e. $k_0 \zeta_0 > 0.4$, accompanied by the intensification of wave breaking leads to the deviation of the distribution of $|\hat{\eta}(k, \omega)|$ from the linear dispersion curve (2.13), cf. Figure 15 (c) and (d). The magnitude of this deviation is dependent on the wave train steepness parameter $k_0 \zeta_0$. Note, the wave train with $k_0 \zeta_0 = 1.0$ is subject to breaking within the entire range of t and x used for computing the $k - \omega$ spectrum. Moreover, the deviation is observed only for the wavenumbers above the spectral peak k_0 , while long waves always follow the linear dispersion. To some extent, this phenomenon is correlated to the phase shift plotted in Figure 12 and 14, which is also present at high wavenumbers only.

The dependency of frequency on the wavenumber $\omega(k)$ can be approximated from the distribution of $|\hat{\eta}(k, \omega)|$ presented in Figure 15 by using the following weighting:

$$\omega(k_n) = \frac{\sum_m \omega_m |\hat{\eta}(k_n, \omega_m)|^2}{\sum_m |\hat{\eta}(k_n, \omega_m)|^2} \quad (4.13)$$

The approximate dispersion relations obtained from the BEM ν and VOF results are plotted in Figure 16 (a) for the steepest wave packet $k_0 \zeta_0 = 1.0$. It is clearly shown that the results of both numerical models deviate from the linear dispersion relation. Meanwhile the deviation is less pronounced for the BEM ν model, implying the importance of including non-potential effects in calculations. Here we attempt to correct the dispersion curve of the BEM ν model by involving the phase shift (4.9) and the expression (4.11):

$$\omega(k) = \omega_{BEM\nu}(k) + \left\langle \frac{\partial \Delta \xi}{\partial t} \right\rangle \approx \omega_{BEM\nu} \left\langle 1 + \Theta_T \Xi \left[\hat{F}_{\hat{x}} \right]^{\Theta_F} \left[\frac{k}{k_0} \right]^{\Theta_K} \left[\frac{t}{T_0} \right]^{\Theta_T - 1} \right\rangle \quad (4.14)$$

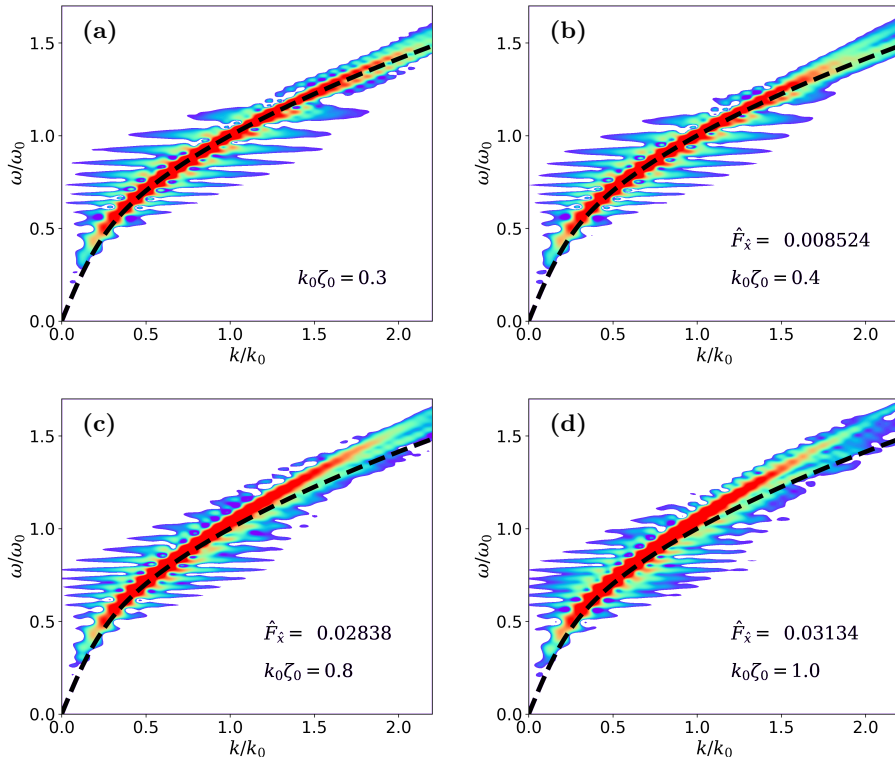


FIGURE 15. Dimensionless free wave k - ω spectrum $|\hat{\eta}(k, \omega)| / \max(|\hat{\eta}(k, \omega)|)$ obtained from the VOF simulations for wave packets with different steepness. The logarithmic color scale has the range $|\hat{\eta}| / \max(|\hat{\eta}|) = [3 \times 10^{-3}, 3 \times 10^{-1}]$. Dashed line represents the linear dispersion curve (2.13) with accounted capillary effects.

Taking into account $(\Theta_T - 1) \sim 0$, the expression (4.14) can be simplified as:

$$\omega(k) = \omega_{BEM\nu} \left(1 + \Theta_T \Xi \left[\hat{F}_{\hat{x}} \right]^{\Theta_F} \left[\frac{k}{k_0} \right]^{\Theta_K} \right) \quad (4.15)$$

The corrected dispersion curve (4.15) for the BEM ν model plotted in Figure 16 (a) is close to the VOF model. This suggests that the difference in wave dispersion between the two models is caused by the phase shift phenomenon discussed in Section 4.3.

The dependency of phase speed on the wavenumber $c_p(k) = \omega/k$ is studied in Figure 16 (b). Linear and BEM ν dispersions show significant variation of the value of c_p within the considered range of the wavenumbers. On the other hand, the VOF data suggests a constant value of c_p at high wavenumbers. This implies that relatively short waves propagate at a similar speed. Note that capillarity in (2.13) has an insignificant effect within the considered range of wavenumbers. Contrary to the observations of Houtani *et al.* (2018*b,a*), the property $c_p \neq c_p(k)$ is only held for high wavenumbers in the considered case.

4.5. Wave train trajectory

As demonstrated in Section 4.4, wave breaking can cause high-frequency harmonics to propagate at a speed appreciably greater than that defined by the linear dispersion relation (2.13). Under these circumstances, short wave components propagate together

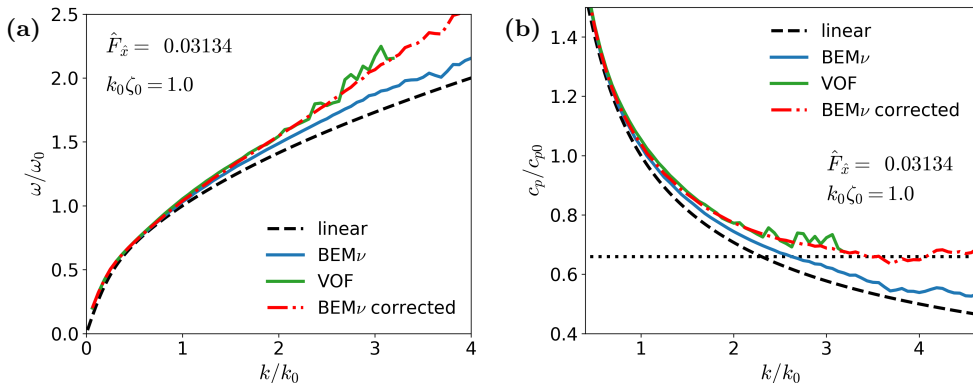


FIGURE 16. Dependence of (a) angular frequency and (b) phase speed on the wavenumber obtained from the results of BEM ν and VOF simulations using (4.12) and (4.13). The correction to the BEM ν curve is obtained using (4.15). Wave train with the steepness parameter $k_0\zeta_0 = 1.0$ is considered in the plots.

with longer ones, thus preventing the dispersive spreading of wave packet. Such an evolution can lead to the distortion of wave train shape and spatio-temporal energy redistribution. Besides, the propagation speed of the entire wave packet can also be influenced by wave breaking nonlinearities. The propagation speed of wave packet energy in space is defined by the group velocity. Consider group velocity of the carrier (peak) frequency harmonic by differentiation of (4.15):

$$c_{g0} = \left. \frac{\partial \omega}{\partial k} \right|_{k=k_0} \approx c_{g0, BEM\nu} \left(1 + \Theta_T \Xi \left[\hat{F}_x \right]^{\Theta_F} \right) \quad (4.16)$$

The expression (4.16) suggests that the wave train propagation velocity increases with breaking intensity defined by the energy dissipation rate \hat{F}_x . In this section, the dynamics of the wave packet evolution is studied to verify these hypotheses.

The propagation velocity of a wave train can be evaluated by analysing the surface elevation envelope obtained from numerical simulations. At each instant t , the Hilbert transform is applied to calculate wave train envelopes from free wave surface elevations $\eta(x, t)$ obtained by the BEM ν and VOF models:

$$\mathcal{H}(x) = \left| \eta(x) + \frac{i}{\pi} \text{PV} \int_{-\infty}^{+\infty} \frac{\eta(\chi)}{\chi - x} d\chi \right|, \quad (4.17)$$

and the dimensionless form is given by:

$$\tilde{\mathcal{H}}(x, t) = \frac{\mathcal{H}(x, t)}{\max_{x, t}(\mathcal{H}(x, t))} \quad (4.18)$$

In the limit of linear system, the velocity of a Gaussian wave train is determined by the propagation speed of the envelope maximum. When waves become highly nonlinear, the instantaneous envelope is disturbed by the fast variations due to nonlinear interactions, which redistribute the energy \mathcal{H}^2 within the wave train. Since these variations do not determine the mean velocity of the energy propagation, the linear approach is not applicable. There is no strict method yet to determine the propagation speed of a strongly nonlinear wave packet. In this study the wave train trajectory in the $x - t$ space is

evaluated by using a central weighting of the energy distribution:

$$X_H(t) = \frac{\sum_x x \tilde{\mathcal{H}}^2(x, t)}{\sum_x \tilde{\mathcal{H}}^2(x, t)}, \quad (4.19)$$

where $X_H(t)$ is the instantaneous wave train coordinate. The instantaneous propagation speed of the wave train is then $v(t) = dX_H/dt$.

The distribution of $\tilde{\mathcal{H}}(x, t)$ obtained by the BEM ν model is plotted in Figure 17 for wave trains with different steepness. Note that the x coordinates are displaced by the linear focus location x_f and transformed using the linear group velocity of the wave packet. For the purpose of analysis, the range of x coordinates containing the dominant portion of the energy and determining the wave train boundaries is chosen by using the condition $\tilde{\mathcal{H}}^2 \geq 0.1$ as depicted by solid lines in Figure 17. The distance between these boundaries can be used as a measure of the wave train instantaneous length $L_H(t)$, see panels (e) and (f).

The spectrum of weakly-nonlinear wave train varies slowly so that its shape is conserved within the time intervals considered in the study. The peak values and the spectral-weighted group velocities (4.4) are thus very close to each other, i.e. $c_{g0} \approx c_{gs}$. Consequently the value of c_{g0} gives a reasonable estimation of the wave packet propagation speed. Thus the wave train trajectory is aligned with the vertical axis as shown in Figure 17 (a), where the wave train has a low steepness $k_0\zeta_0 = 0.2$. The actual focal point for this case practically coincides with the linear prediction shown in the figure by dotted lines. Increasing the steepness to $k_0\zeta_0 \geq 0.3$ changes the free surface elevation envelope. The wave train trajectory $X_H(t)$ (4.19) is plotted by the dashed lines in Figures 17 (c)-(f). It is shown that the intensification of wave breaking (growth of $k_0\zeta_0$ and \hat{F}_x) leads to the inclination of wave train trajectory $X_H(t)$ from the vertical line, cf. panels (a)-(f). For the cases with relatively strong energy dissipation, i.e. $k_0\zeta_0 \geq 0.6$, the plots of $X_H(t)$ after the focal point are almost linear. This suggests that for each of these cases, breaking increases the wave packet propagation velocity $v(t) = dX_H/dt$ by a constant value equal to the gradient of the straight line.

The evolution of weakly-nonlinear wave train, see Figure 17 (a), consists of two consecutive stages: (I) focusing within the time interval $t = 30 - 35$ s, and (II) defocusing (dispersive spreading) within $t = 35 - 40$ s. Breaking is only expected to occur in the vicinity of the focal point at $t = 35$ s. Although the surface elevation envelopes of moderately nonlinear wave packets are distorted, both the focusing and defocusing stages are still clearly present, cf. Figures 17 (b) and (c). However, the occurrence of multiple stronger breakers modifies significantly the envelope evolution process for the cases with high steepness $k_0\zeta_0 \geq 0.6$, for which a defocusing stage is no longer clearly visible in panels (d)-(f).

In view of similarity in the propagation regime of breaking wave trains, we consider the strongest energy dissipation case shown in Figure 17 (f). This wave train exhibits appreciable energy dissipation due to the strong and nearly continuous breaking within the full time range studied here, as clearly shown in Figures 4 and 8. Despite this, the focusing stage is still largely pronounced. On the contrary, surprisingly, the spreading of wave train in the post-focusing stage is completely suppressed, cf. Figures 17 (d)-(f). Therefore, the reduction of wave height due to dispersion is less pronounced than the low steepness cases presented in panels (a)-(c). This suggests that once extreme breaking waves appear, they propagate together without spreading until breaking dissipates the excessive energy and ceases. It also implies that such extreme waves could last longer than

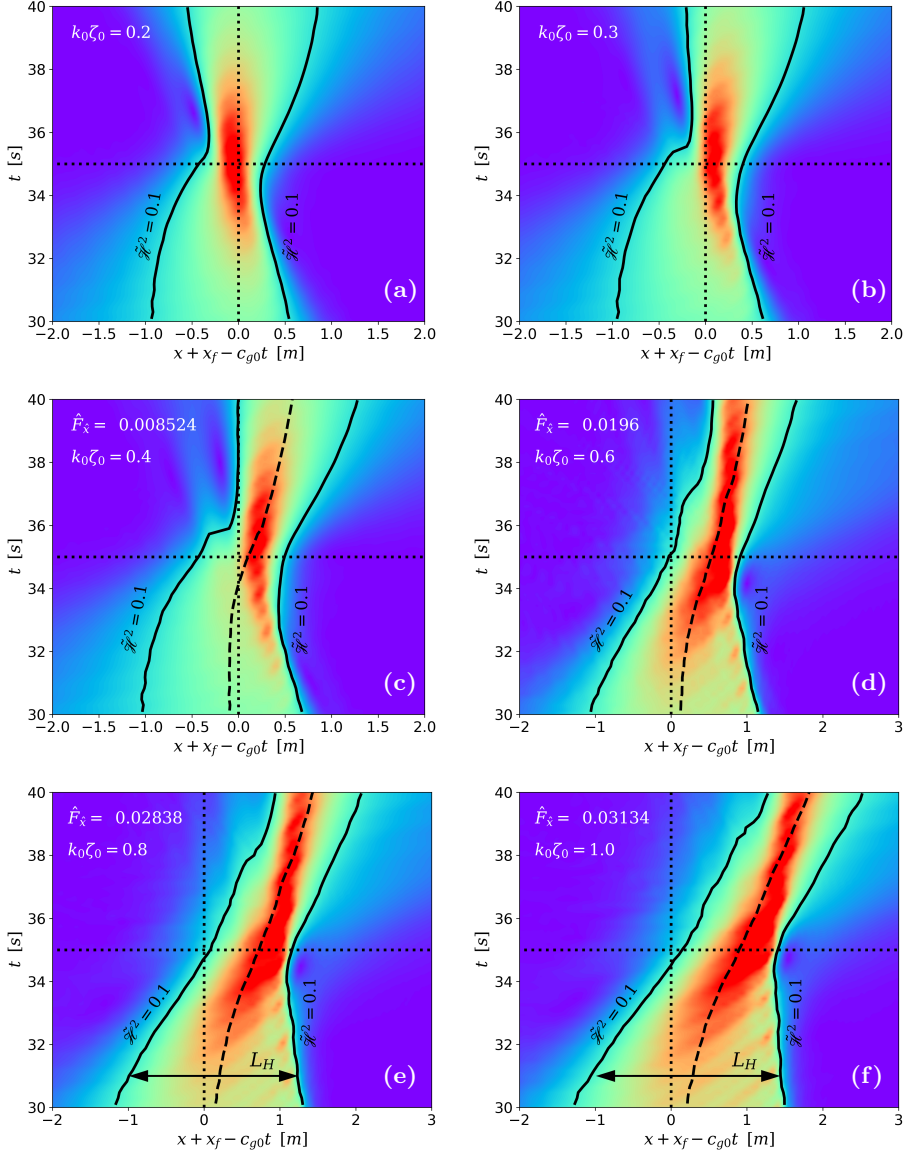


FIGURE 17. Surface elevation envelope $\tilde{\mathcal{H}}(x, t)$ (4.18) in x - t space obtained from the results of BEM ν computations: (a)-(f) present the wave trains of different steepness $k_0\zeta_0$. The color scale has the range $0 \leq \tilde{\mathcal{H}} \leq 0.8$; higher values ($\tilde{\mathcal{H}} > 0.8$) are shown by red color. The boundaries of the wave train corresponding to the energy level $\tilde{\mathcal{H}}^2 = 0.1$ are plotted by solid lines. Dotted lines depict the linear focal point location. The approximate wave train coordinates $X_H(t)$ (4.19) are plotted by dashed lines. The instantaneous wave train length $L_H(t)$ is indicated in panels (e) and (f).

expected. Having a close look at the red areas shown in Figure 17, where $\tilde{\mathcal{H}}(x, t) \geq 0.8$, we can clearly see their growth in time with wave train steepness especially for $k_0\zeta_0 \geq 0.6$. For low steepness wave trains $k_0\zeta_0 \leq 0.4$, the wave height reduces to less than 50% of the maximum height by time $t = 38$ s. But for highly nonlinear waves $k_0\zeta_0 \geq 0.6$, the red regions can extend beyond $t = 40$ s. This means that increasingly intensified breaking

can prolong the lifespan of extreme waves, and such an effect may not necessarily be trivial.

The surface elevation envelopes computed by the VOF model for non-breaking wave packets ($k_0\zeta_0 = 0.2$ and 0.3) coincide with the BEM ν results, cf. Figures 17 and 18 panels (a) and (b). The distributions of $\mathcal{H}(x, t)$ elicited from the VOF simulations for breaking wave trains with $k_0\zeta_0 \geq 0.4$ are presented in Figure 18 (c)-(f). Similar to the BEM ν computations, the evolution of non-breaking and weakly-breaking wave trains consists of both dispersive focusing and defocusing stages, while there is no clear defocusing stage for strongly-breaking cases in the domain of interest, cf. Figures 17 and 18. At the same time, the wave train boundaries obtained by the VOF model become rough with the intensification of breaking due to the generation of rotational flow components.

The wave train trajectories $X_H(t)$ (4.19) obtained by the VOF model are plotted in Figure 18 with dash-dotted lines. Corresponding plots of $X_H(t)$ taken for reference from Figure 17 (BEM ν) are shown by dashed lines. In the focusing stage, the trajectories of weakly-breaking wave trains computed by the BEM ν and VOF models are very close to each other as shown in Figure 18 (c). Once breaking is initiated in the vicinity of the focal point, a small divergence of the trajectories appears. For strong breaking events as shown in Figure 18 (d)-(f), the divergence in wave trajectory between the VOF and BEM ν models becomes appreciably large. Wave trains computed by the VOF model propagate over longer distances and thus have higher propagation speeds compared to the BEM ν outcomes. These observations confirm our initial assumption that breaking can increase the propagation speed of wave trains compared to non-breaking scenarios. And this is associated with the phase shifting phenomenon as demonstrated in (4.16). The non-potential flow components generated by multiple breaking events, not taken into account in the BEM ν computations, could be responsible for such speed growth. For instance, the breaking-induced sheared current varying in both time and space (Deike *et al.* 2017; Lenain *et al.* 2019) may have a significant nonlinear effect on the propagation speed.

Applying linear regression to the trajectories $X_H(t)$ derived from BEM ν and VOF computations, the wave group propagation velocity $v(t) = dX_H/dt$ is estimated numerically and plotted in Figure 19. The linear group velocity c_{g0} calculated by using the spectral carrier frequency is included here for reference. Strongly-nonlinear but non-breaking wave trains ($\hat{F}_{\hat{x}} \approx 0$) propagate at a speed moderately higher than the linear group velocity c_{g0} . The growth of propagation speed in this case is caused by nonlinear resonant interactions between the spectral harmonics. A similar outcome has been obtained analytically by Stuhlmeier & Stiassnie (2019) for nonlinear waves of Pierson–Moskowitz spectra. Significant increases in the propagation speed can be clearly seen for the breaking waves ($\hat{F}_{\hat{x}} > 0$), which may attain the following values: $v_{BEM\nu} \approx 1.27c_{g0}$ and $v_{VOF} \approx 1.36c_{g0}$. While the growth observed in BEM ν computations is mostly related to the nonlinearities in the free-surface boundary conditions (2.2) and (2.3), the additional increment of speed present in the VOF model is likely caused by breaking-induced rotational flows.

It is known that the balance of spectral energy in wave forecasting models is closely dependent on wave group velocity, which is usually approximated by the linear dispersion relation (2.13). Stuhlmeier & Stiassnie (2019) pointed out that a more accurate nonlinear approximation of the group velocity derived from the Zakharov equation is needed. This means the complex effect of wave breaking on modifying group velocity is of practical importance and needs to be taken carefully into account.

Figure 20 exhibits the temporal evolution of wave group length L_H , which is defined as the distance between the leading and trailing edges of a wave train, as shown in Figures 17 and 18. The wave group length is normalised by its value taken at $t =$

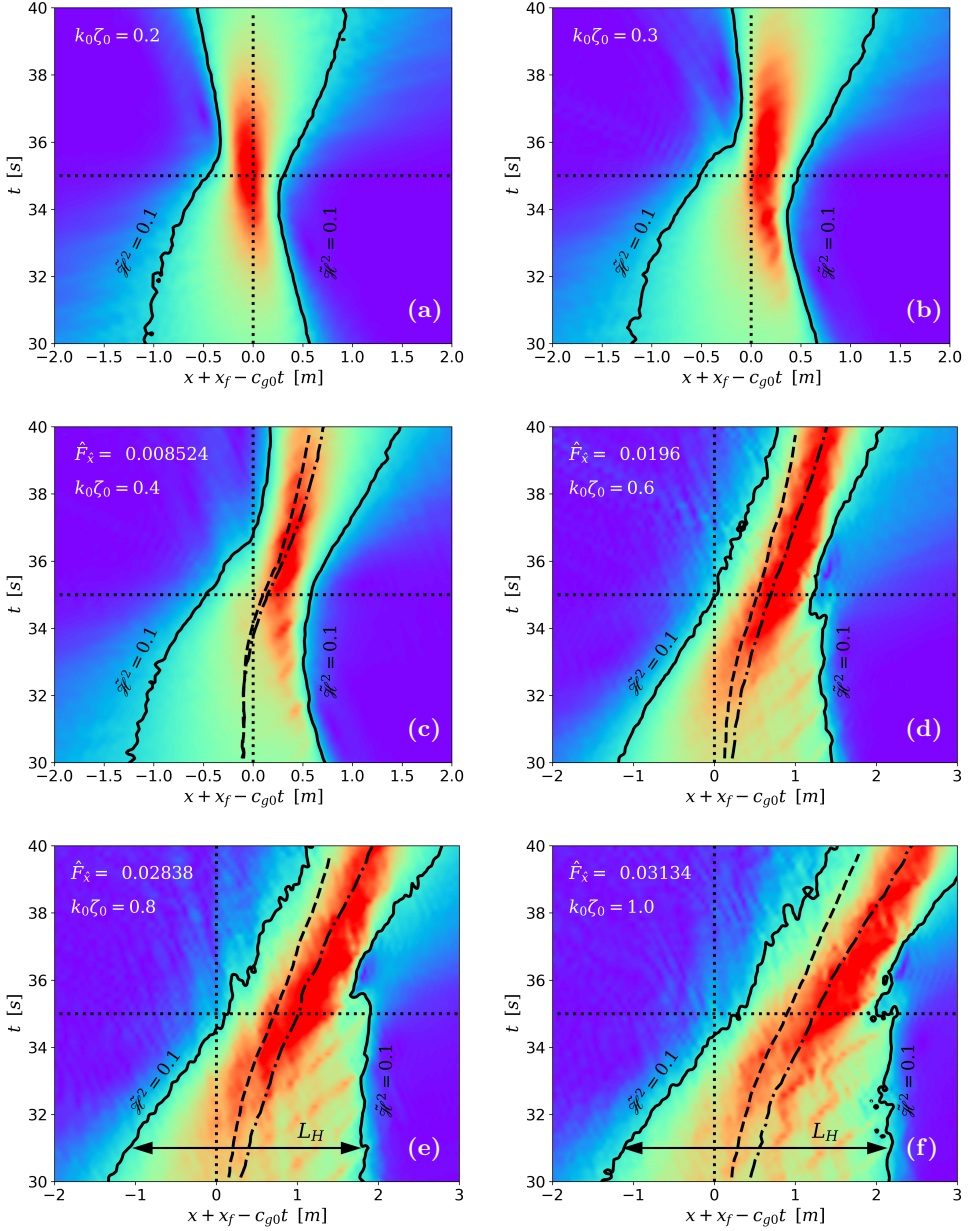


FIGURE 18. As in Figure 17 for VOF model. Dashed and dash-dotted lines show $X_H(t)$ calculated from BEM ν and VOF simulation results, respectively.

30 s when wave generation is completed in both BEM ν and VOF models. As discussed above, all non-breaking and weakly-breaking wave trains ($0.2 \leq k_0\zeta_0 \leq 0.4$) are subject to consequent focusing and defocusing stages due to dispersion. For a strong breaking wave with $k_0\zeta_0 \geq 0.6$, the defocusing stage is suppressed, cf. Figure 20 (a) and (b). More importantly, the relative wave packet lengths after focusing are nearly constant and have similar magnitude in both BEM ν and VOF computations: $L_H/L_{H0} = \text{const} \in [0.45, 0.5]$. The wave packet spreading is expected to resume after the breaking process is completed.

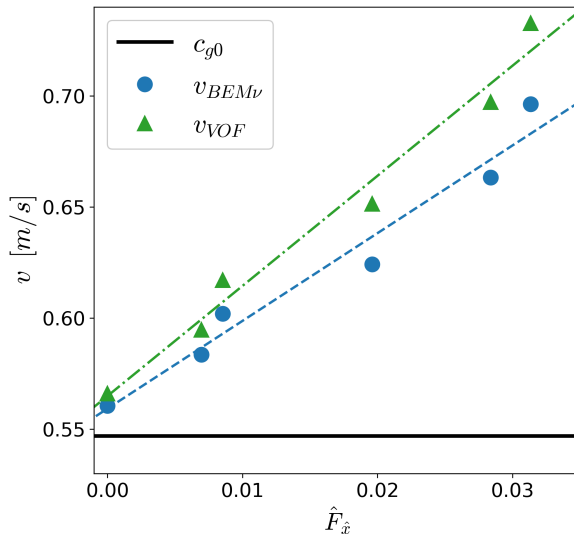


FIGURE 19. Dependence of the wave train propagation velocity $v(t) = dX_H/dt$ on the energy dissipation rate $\hat{F}_{\hat{x}}$ (i.e. wave breaking strength). Dashed and dash-dotted lines represent the linear fit of the data derived from BEM ν and VOF computations.

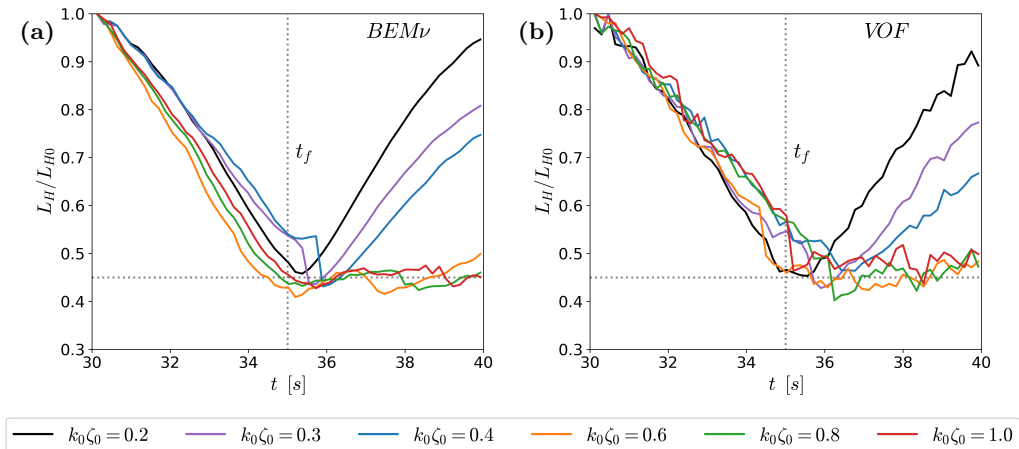


FIGURE 20. Evolution in time of the normalised length of the non-breaking to strongly-breaking wave trains: (a) BEM ν and (b) VOF computations. Definition of the wave train length is shown schematically in figures 17 and 18; L_{H0} is the initial wave train length.

However, the absolute values of wave group length computed by the BEM ν and VOF models are different because of the wave evolution peculiarities during the focusing stage.

It has been reported that wind has a pronounced effect of amplifying wave height for broad-banded focusing wave groups in the defocusing stage (Touboul *et al.* 2008; Chambarel *et al.* 2010). It is also of interest and importance to analyse the height amplification effect of wave breaking through the non-dimensional factor given by:

$$\tilde{H}(t) = \frac{2 \times \max\{\mathcal{H}(x, t)\}}{H_S(k_0 \zeta_0 = 0.4)} \quad (4.20)$$

Here we introduce the normalisation by using the constant significant wave height H_S calculated for the wave train at the verge of stability, i.e. weakly-breaking group with $k_0\zeta_0 = 0.4$. Following the standard definition (Babanin *et al.* 2011), significant wave height can be calculated from (2.15):

$$H_S \equiv 4\sqrt{\frac{1}{2\pi} \int_{-\infty}^{+\infty} \hat{\eta}^2(\omega) d\omega} = \sqrt[4]{\frac{8}{\pi} \sqrt{m\zeta_0^2 T_0 (1 + e^{-2\pi^2 m^2})}} \quad (4.21)$$

The factor of 2 is introduced into the numerator of (4.20) to evaluate the expected wave height from the envelope \mathcal{H} . Figure 21 shows the temporal evolution of wave height amplification factor defined by the expression (4.20). Linear regression is applied in panel (b) separately to the focusing ($t < 35$ s) and defocusing ($t > 35$ s) stages. It is clearly shown that the amplification of the non-breaking wave group ($k_0\zeta_0 = 0.2$) is nearly symmetric about the focal point. Increase of the steepness parameter $k_0\zeta_0$ causes certain asymmetry of \tilde{H} in the pre- and post-focusing stages, see panel (a).

It is usually expected that strong breaking leads to instantaneous reduction of the wave height. However, Figure 21 (b) demonstrates a quite opposite and nontrivial phenomenon. The height amplification factors of strongly-breaking wave groups, in particular the solution for $k_0\zeta_0 \geq 0.6$, decay much slower than the non-breaking and weakly-breaking ones, cf. panels (a) and (b). This is probably due to the suppression of defocusing and the consequent conservation of wave train length shown in Figure 20. Both VOF and BEM ν models demonstrate asymmetry of \tilde{H} plots in the pre- and post-focusing stages with the increase of wave steepness especially when breaking is initiated.

Under strong breaking conditions, see panel (b), the peak values of \tilde{H} produced by the BEM ν model are higher than the VOF calculations for each wave train. Unlike the BEM ν model which shows significant decay rate of \tilde{H} in the post-focusing stage regardless of wave train steepness, the VOF solutions demonstrate a very mild decay of \tilde{H} over time for $k_0\zeta_0 \geq 0.6$. It is crucial to emphasize that such conservation of \tilde{H} with time could be due to the impact of breaking generated rotational flows and currents in the water mass, which decay slowly and can remain in the flow for several wave periods or even longer. This implies that breaking induced rotational flows and currents, completely disregarded in the BEM ν model, may play an important role in formation of extremely high waves. Such observation may find a confirmation in (Toffoli *et al.* 2019).

The implication of the phenomenon discussed above is that the space (range of x) where extreme waves are likely to appear might be expanded as compared to FNP predictions. For very steep wave trains $k_0\zeta_0 \geq 0.8$, their amplification factors remain above 2.2 for a relatively long time in the post-focusing stage as shown in Figure 21 (b). But in the pre-focusing stage, such large values can only be seen in the vicinity of the focal point. In this sense, the occurrence probability and lifespan of extreme waves might be increased by frequent and violent breakings.

5. Conclusions

A suite of low-fidelity (FNP) and coupled low-/high-fidelity (FNP-NS) flow models have been proposed to investigate the evolution of broad-banded wave trains under non-, moderate- and strong-breaking conditions. The weakly-potential approximation proposed by Ruvinsky *et al.* (1991) was implemented in the FNP model to take into account the energy dissipation caused by wave breaking. This approximation was closed by the eddy viscosity model proposed by Tian *et al.* (2010, 2012).

The developed flow models were firstly tested with a wave train subject to modulational

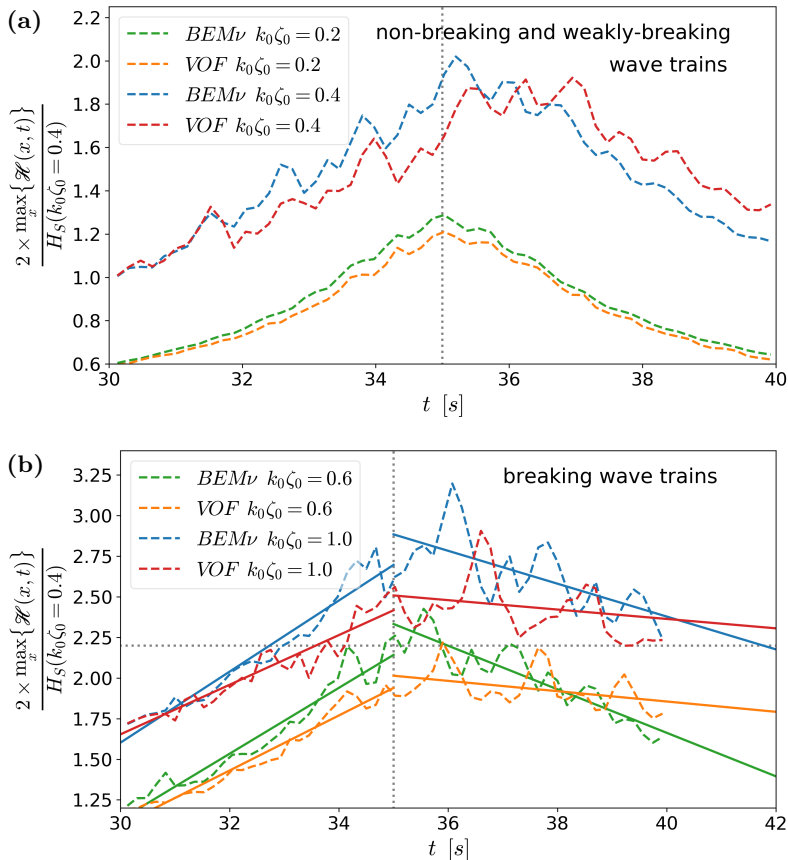


FIGURE 21. Evolution of the amplification factor \tilde{H} (4.20) observed in $BEM\nu$ and VOF computations: (a) non- and weakly-breaking wave trains, (b) strongly-breaking wave trains. Dashed lines present the raw data derived from the computations, while solid lines are obtained by the linear interpolation of the plots separately at focusing and defocusing stages. Vertical dotted line shows focal point location at $t = 35$ s.

instability. Within the FNP model we also applied the free surface re-meshing technique, which shows a similar performance as the eddy viscosity enclosure in the stabilisation of breaking wave simulation. The computed results were compared with laboratory measurements and other published calculations in terms of surface elevation. It was found that the high-fidelity results compare well with experiments. Although the low-fidelity calculations are rather close to the high-order-spectral solutions reported in the literature, they deviate from laboratory measurements especially at locations far away from the wave maker.

To identify the underlying reason causing the deficiency of the eddy viscosity wave breaking model in the prediction of surface elevation, we further examined the FNP and FNP-NS models with six broad-banded focusing wave groups under non-, moderate- and strong-breaking conditions. A direct comparison of the low- and high-fidelity results reveals that the re-grid and eddy viscosity approaches predict accurately the energy dissipation caused by breaking. We then applied spectral decomposition to compute the surface elevation of free waves by filtering out bound waves. Surprisingly, it was found that the amplitude spectra obtained from the FNP and NS solutions are practically identical

in terms of magnitude, regardless of wavenumber and angular frequency. This led us to speculate that the underlying reason causing the deviation of FNP solutions from high-fidelity calculations (and laboratory measurements) in terms of surface elevation is the discrepancy in phase.

To verify this hypothesis, we undertook a detailed analysis of the phase difference between the FNP and NS results. It was found that the difference in phase grows with breaking intensity, and such an effect is especially profound for high wavenumber components. We proposed an empirical formula to correlate the phase shift with wavenumber, energy dissipation rate and time in the power form by applying regression to the data. For strongly breaking wave trains it was found that the phase shift has a quadratic dependence on energy dissipation rate and wavenumber. Moreover, the shift of phase occurs at relatively high wavenumbers, but is hardly observed for long waves. It was also noticed that the growth of phase shift with time is nearly linear for strongly breaking waves. It is suggested that the observed variation in phases has similar physical origin as phase-locking effect reported by Derakhti & Kirby (2016). Therefore, phase-locking is considered to be the main reason for inaccuracy of FNP predictions.

The proposed phase shift regression function was then used to study the dispersive property of breaking wave trains. It was found that weak breaking has very limited impact on the dispersion of fully-nonlinear wave packets. On the contrary, strong breaking has great influence on the dispersive property of wave packets, causing the frequencies of high wavenumber components to increase significantly. This phenomenon has been clearly demonstrated by using a 2D Fourier transform of the high-resolution spatio-temporal records of surface elevation. We also showed that the dispersion variation can be derived from the phase shift regression function. This suggests that the shift of phase could be a cause of dispersion variation. We would like to emphasise that the complex phenomena of phase shift and dispersion change may be caused by a combined action of the nonlinear interaction of resonant waves as well as the breaking-induced rotational flows.

The change of wave dispersion caused by breaking increases the propagation speed of high wavenumber components. In the NS computation of strongly breaking waves, the phase speeds of high wavenumber components tend to be independent of the wavenumber i.e. these harmonics propagate at a similar speed. As a result, the dispersive spreading of wave train after the focal point is almost absent in all simulations of strongly breaking waves. It was found that the evolution of wave trains involving strong breaking consists of two distinctive stages: (1) a contraction of the wave train length and an accompanying growth of the wave height due to focusing; and (2) maintaining a nearly constant wave train length after the focal point instead of spreading out instantly as usually expected. This unusual conservation of wave train length is of significance because it can prolong the lifespan of focused waves and expand the space for their propagation. This can raise the probability of extreme wave formation in breaking scenarios compared to non-breaking environments. Such an unexpected finding is contradictory to our general impression that strong breaking can instantly reduce wave height by destructing initially stable harmonics and dissipating their mechanical energy.

We would like to emphasise that in the current stage the conclusions drawn here are based on, and possibly limited to, the quantitative analysis of the wave trains considered in the present work. More comprehensive theoretical, numerical and experimental investigations are needed to arrive at definitive conclusions on phase shifting and other related phenomena reported in this paper. The outcomes of the current research can be beneficial to the development of more accurate theoretical models for wave breaking, which can be used in the weakly- and fully-nonlinear modelling of ocean waves for engineering and environmental science.

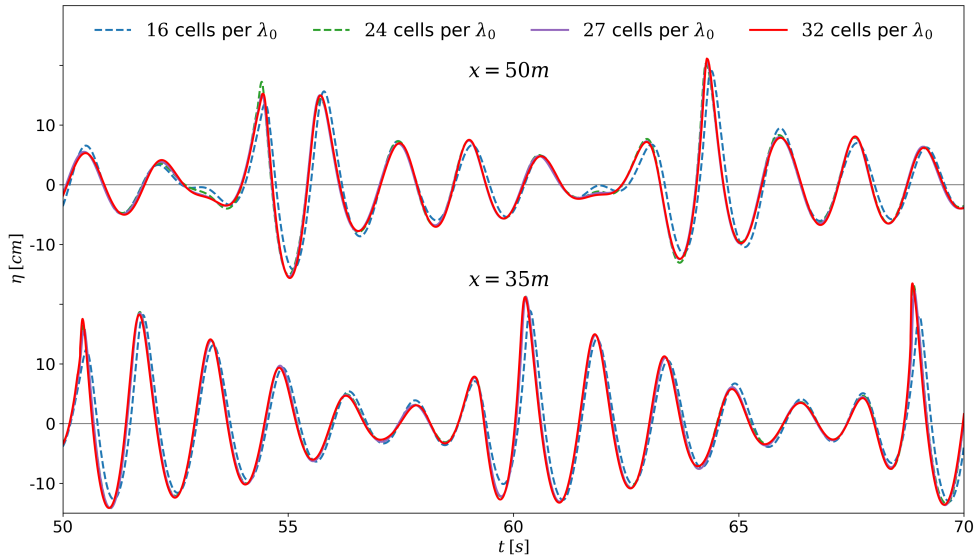


FIGURE 22. Surface elevation obtained in BEM ν computations at two coordinates measured from the wavemaker location: $x = 35m$ and $x = 50m$.

Acknowledgements

This work was supported by the Engineering and Physical Sciences Research Council (EPSRC), U.K. Project: High-fidelity Simulation of Air Entrainment in Breaking Wave Impacts, under Grant No. EP/S011862/1. The authors would also like to express gratitude to Professor Lev Shemer from Tel Aviv University, Israel for his encouragement and constructive advice helping us to improve the quality of the manuscript.

Appendix A. Grid convergence

The grid convergence of BEM ν and VOF numerical models is studied with respect to the modulated wave train (2.12). The grid density determined as number of cells (nodes) distributed along the carrier wave length λ_0 is used for characterisation of the grid quality. This allows generalisation of the convergence study outcomes to other wave trains investigated in the paper. Four grids of different free surface mesh density ranging from 16 to 32 cells per λ_0 are considered in the BEM ν model, see Figure 22. All meshes show identical surface elevation plots close to the wavemaker ($x = 35m$), as well as far away from it ($x = 50m$). Nevertheless, the finest mesh is used in the present work.

The grid resolutions of 64 to 256 cells per carrier wave length λ_0 were considered in convergence study of the VOF model, see Figure 23. In this case, first two grids fail in simulation of the waves dispersion. The grid densities 192 and 256 cells per λ_0 showed practically identical results at $x = 35m$. Deviation between the results obtained with these two grids at $x = 50m$ is acceptably small, thus the convergence is established with respect to the free surface elevation. The finest grid of density 256 cells per λ_0 is used for the computations.

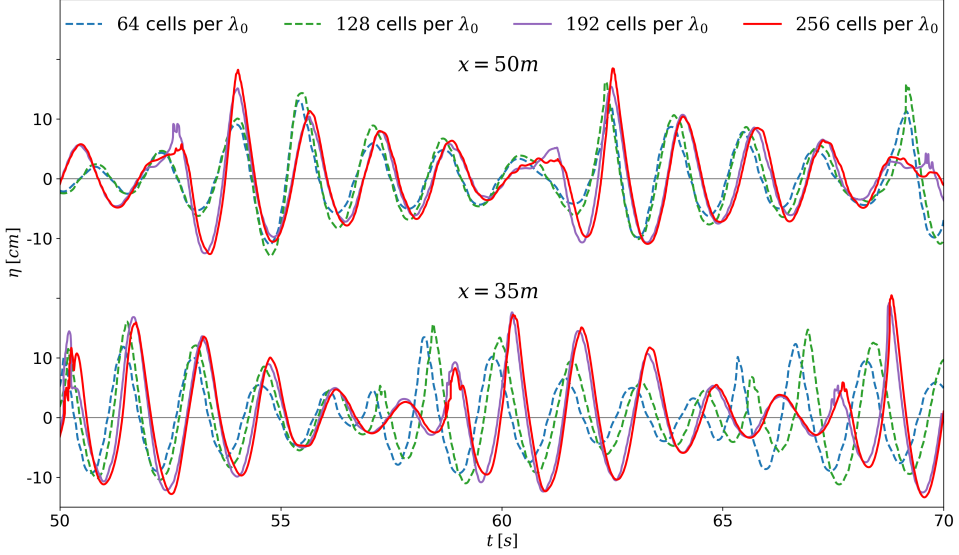


FIGURE 23. As in Figure 22 for the results of VOF computations.

Appendix B. Coefficients of the weakly-nonlinear Zakharov model

Assume $A(k)$ being the discrete complex wavenumber spectrum of the free waves only. Introduce the following wavenumbers:

$$k_b = k_m + k_n \quad \text{and} \quad k_c = -k_m + k_n \quad \text{and} \quad k_d = -k_m - k_n \quad (\text{B1})$$

The corresponding angular frequencies due to dispersion relation (2.13) are:

$$\omega_b = \sqrt{gk_b \tanh(k_b h)} \quad \text{and} \quad \omega_c = \sqrt{gk_c \tanh(k_c h)} \quad \text{and} \quad \omega_d = \sqrt{gk_d \tanh(k_d h)} \quad (\text{B2})$$

The complex wavenumber amplitudes in the 2nd-order bound waves spectrum required to complete expression (2.20) are (Stiassnie & Shemer 1987; Krasitskii 1994):

$$B(k_m, k_n) = -\pi \sqrt{\frac{2g\omega_b}{\omega_m\omega_n}} \frac{V(\omega_b, \omega_m, \omega_n, k_m + k_n, k_m, k_n)}{\omega_b - \omega_m - \omega_n} A_m A_n \quad (\text{B3})$$

$$C(k_m, k_n) = -\pi \sqrt{\frac{2g\omega_c}{\omega_m\omega_n}} \frac{W(\omega_c, \omega_m, \omega_n, -k_m + k_n, k_m, k_n)}{\omega_c + \omega_m - \omega_n} A_m^* A_n \quad (\text{B4})$$

$$D(k_m, k_n) = -\pi \sqrt{\frac{2g\omega_d}{\omega_m\omega_n}} \frac{T(\omega_d, \omega_m, \omega_n, -k_m - k_n, k_m, k_n)}{\omega_d + \omega_m + \omega_n} A_m^* A_n^* \quad (\text{B5})$$

Here m and n are numbers of harmonics in the discrete free waves complex spectrum $A(k)$; the star superscript “*” stands for the complex conjugation. The expressions for the coefficients V , W and T are (Stiassnie & Shemer 1987):

$$V(\omega_0, \omega_1, \omega_2, k_0, k_1, k_2) = \frac{1}{4\pi} \sqrt{\frac{g}{2}} \left\{ \frac{1}{2} \sqrt{\frac{\omega_0}{\omega_1\omega_2}} \left[\left(\frac{\omega_1\omega_2}{g} \right)^2 + k_1 k_2 \right] - \sqrt{\frac{\omega_2}{\omega_0\omega_1}} \left[\left(\frac{\omega_0\omega_1}{g} \right)^2 - k_0 k_1 \right] \right\} \quad (\text{B6})$$

$$\begin{aligned}
W(\omega_0, \omega_1, \omega_2, k_0, k_1, k_2) = & \frac{1}{4\pi} \sqrt{\frac{g}{2}} \left\{ \sqrt{\frac{\omega_2}{\omega_0\omega_1}} \left[\left(\frac{\omega_0\omega_1}{g} \right)^2 + k_0k_1 \right] \right. \\
& \left. - \sqrt{\frac{\omega_1}{\omega_0\omega_2}} \left[\left(\frac{\omega_0\omega_2}{g} \right)^2 - k_0k_2 \right] - \sqrt{\frac{\omega_0}{\omega_1\omega_2}} \left[\left(\frac{\omega_1\omega_2}{g} \right)^2 - k_1k_2 \right] \right\}
\end{aligned} \tag{B7}$$

$$\begin{aligned}
T(\omega_0, \omega_1, \omega_2, k_0, k_1, k_2) = & \frac{1}{4\pi} \sqrt{\frac{g}{2}} \left\{ \sqrt{\frac{\omega_2}{\omega_0\omega_1}} \left[\left(\frac{\omega_0\omega_1}{g} \right)^2 + k_0k_1 \right] \right. \\
& \left. + \frac{1}{2} \sqrt{\frac{\omega_0}{\omega_1\omega_2}} \left[\left(\frac{\omega_1\omega_2}{g} \right)^2 + k_1k_2 \right] \right\}
\end{aligned} \tag{B8}$$

REFERENCES

- ANNENKOV, SERGEI Y. & SHRIRA, VICTOR I. 2018 Spectral evolution of weakly nonlinear random waves: kinetic description versus direct numerical simulations. *J. Fluid Mech.* **844**, 766–795.
- BABANIN, ALEXANDER V. 2011 *Breaking and dissipation of ocean surface waves*. Cambridge University Press.
- BABANIN, ALEXANDER V. & CHALIKOV, DMITRY 2012 Numerical investigation of turbulence generation in non-breaking potential waves. *J. Geoph. Res.* **117**, C06010.
- BABANIN, A. V., WASEDA, T., KINOSHITA, T. & TOFFOLI, A. 2011 Wave breaking in directional fields. *J. Phys. Ocean.* **41**, 145–156.
- BANNER, MICHAEL L. & PEIRSON, WILLIAM L. 2007 Wave breaking onset and strength for two-dimensional deep-water wave groups. *J. Fluid Mech.* **585**, 93–115.
- CHALIKOV, DMITRY & BABANIN, ALEXANDER V. 2014 Simulation of one-dimensional evolution of wind waves in a deep water. *Phys. Fl.* **26**, 096607.
- CHALIKOV, DMITRY & SHEININ, DMITRY 2005 Modeling extreme waves based on equations of potential flow with a free surface. *J. Comput. Phys.* **210**, 247–273.
- CHAMBAREL, J., KHARIF, C. & KIMMOUN, O. 2010 Generation of two-dimensional steep water waves on finite depth with and without wind. *Eur. J. Mech. B Fluids* **29**, 132–142.
- CRACIUNESCU, CONSTANTIN COSMIN & CHRISTOU, MARIOS 2020 Wave breaking energy dissipation in long-crested focused wave groups based on jonswap spectra. *Applied Ocean Research* **99**, 102144.
- DE VITA, FRANCESCO, VERZICCO, ROBERTO & IAFRATI, ALESSANDRO 2018 Breaking of modulated wave groups: kinematics and energy dissipation processes. *J. Fluid Mech.* **855**, 267–298.
- DEAN, R.G. & DALRYMPLE, R.A. 1991 *Water Wave Mechanics for Engineers and Scientists*. World Scientific, Singapore.
- DEIKE, LUC, PIZZO, NICK & MELVILLE, W. KENDALL 2017 Lagrangian transport by breaking surface waves. *J. Fluid Mech.* **829**, 364–391.
- DERAKHTI, MORTEZA & KIRBY, JAMES T. 2016 Breaking-onset, energy and momentum flux in unsteady focused wave packets. *J. Fluid Mech.* **790**, 553–581.
- DIAS, F., DYACHENKO, A.I. & ZAKHAROV, V.E. 2008 Theory of weakly damped free-surface flows: A new formulation based on potential flow solutions. *Physics Letters A* **372** (8), 1297–1302.
- DOSAEV, A., TROITSKAYA, Y.I. & SHRIRA, V.I. 2021 On the physical mechanism of front–back asymmetry of non-breaking gravity–capillary waves. *J. Fluid Mech.* **906**, A11.
- DRAZEN, DAVID A., MELVILLE, W. KENDALL & LENAIN, LUC 2008 Inertial scaling of dissipation in unsteady breaking waves. *J. Fluid Mech.* **611**, 307–332.
- DUCROZET, GUILLAUME, BONNEFOY, FÉLICIEN, LE TOUZÉ, DAVID & FERRANT, PIERRE 2012 A modified high-order spectral method for wavemaker modeling in a numerical wave tank. *Eur. J. Mech. B/Fluids* **34**, 19–34.
- DUCROZET, GUILLAUME, BONNEFOY, FÉLICIEN, LE TOUZÉ, DAVID & FERRANT, PIERRE 2016

- Hos-ocean: Open-source solver for nonlinear waves in open ocean based on high-order spectral method. *Comput. Phys. Commun.* **203**, 245–254.
- GIBSON, R.S. & SWAN, C. 2006 The evolution of large ocean waves: the role of local and rapid spectral changes. *Proc. R. Soc. A.* **463**, 21–48.
- GRILLI, S.T., SKOURUP, J. & SVENDSEN, I.A. 1989 An efficient boundary element method for nonlinear water waves. *Eng. Anal. Boundary Elem.* **6(2)**, 97–107.
- GRILLI, S.T. & SUBRAMANYA, R. 1996 Numerical modeling of wave breaking induced by fixed or moving boundaries. *Comput. Mech.* **17**, 374–391.
- GRILLI, S.T. & SVENDSEN, I.A. 1990 Corner problems and global accuracy in the boundary element solution of nonlinear wave flows. *Eng. Anal. Boundary Elem.* **7**, 178–195.
- HASAN, S.A., SRIRAM, V. & SELVAM, R. PANNEER 2019 Evaluation of an eddy viscosity type wave breaking model for intermediate water depths. *Eur. J. Mech. B Fluids* **78**, 115–138.
- HOUTANI, HIDETAKA, WASEDA, TAKUJI, FUJIMOTO, WATARU, KIYOMATSU, KEIJI & TANIZAWA, KATSUJI 2018a Generation of a spatially periodic directional wave field in a rectangular wave basin based on higher-order spectral simulation. *Ocean Eng.* **169**, 428–441.
- HOUTANI, H., WASEDA, T. & TANIZAWA, K. 2018b Experimental and numerical investigations of temporally and spatially periodic modulated wave trains. *Phys. Fl.* **30**, 034101.
- IAFRATI, A. 2009 Numerical study of the effects of the breaking intensity on wave breaking flows. *J. Fluid Mech.* **622**, 371–411.
- IAFRATI, A., BABANIN, A. & ONORATO, M. 2013 Modulational instability, wave breaking, and formation of large-scale dipoles in the atmosphere. *Phys. Rev. Lett.* **110**, 184504.
- IAFRATI, A., DE VITA, F. & VERZICCO, R. 2019 Effects of the wind on the breaking of modulated wave trains. *Eur. J. Mech. B/Fluids* **73**, 6–23.
- KHAIT, A. & SHEMER, L. 2018 On the kinematic criterion for the inception of breaking in surface gravity waves: Fully nonlinear numerical simulations and experimental verification. *Phys. Fl.* **30**, 057103.
- KHAIT, A. & SHEMER, L. 2019a Application of boundary element method for determination of the wavemaker driving signal. *J. Offshore Mech. Arctic Eng.* **141**, 061102.
- KHAIT, A. & SHEMER, L. 2019b Nonlinear wave generation by a wavemaker in deep to intermediate water depth. *Ocean Eng.* **182**, 222–234.
- KIGER, KENNETH T. & DUNCAN, JAMES H. 2012 Air-entrainment mechanisms in plunging jets and breaking waves. *Ann. Rev. Fl. Mech.* **44**, 563–596.
- KRASITSKII, V.P. 1994 On the reduced equations in the hamiltonian theory of weakly nonlinear surface waves. *J. Fluid Mech.* **272**, 1–20.
- KROGSTAD, H.E. & TRULSEN, K. 2010 Interpretations and observations of ocean wave spectra. *Ocean Dynamics* **60**, 973–991.
- LARSEN, B.E., FUHRMAN, D.R. & ROENBY, J. 2019 Performance of interfoam on the simulation of progressive waves. *Coast. Eng. J.* **61:3**, 380–400.
- LENAIN, LUC, PIZZO, NICK & MELVILLE, W. KENDALL 2019 Laboratory studies of lagrangian transport by breaking surface waves. *J. Fluid Mech.* **876**, R1.
- LUBIN, P & GLOCKNER, S 2015 Numerical simulations of three-dimensional plunging breaking waves: generation and evolution of aerated vortex filaments. *Journal of Fluid Mechanics* **767**, 364–393.
- MA, Z.H., CAUSON, D.M., QIAN, L., MINGHAM, C.G., GU, H.B. & MARTÍNEZ FERRER, P. 2014 A compressible multiphase flow model for violent aerated wave impact problems. *Proc. R. Soc. A.* **470**, 20140542.
- MA, Z.H., CAUSON, D.M., QIAN, L., MINGHAM, C.G. & MARTÍNEZ FERRER, P. 2016 Numerical investigation of air enclosed wave impacts in a depressurised tank. *Ocean Eng.* **123**, 15–27.
- MARTÍNEZ FERRER, P.J., CAUSON, D.M., QIAN, L., MINGHAM, C.G. & MA, Z.H. 2016 A multi-region coupling scheme for compressible and incompressible flow solvers for two-phase flow in a numerical wave tank. *Comput. Fluids* **125**, 116–129.
- MELVILLE, W KENDALL 1996 The role of surface-wave breaking in air-sea interaction. *Annual review of fluid mechanics* **28** (1), 279–321.
- OLIVEIRA, P.J. & ISSA, R.I. 2001 An improved PISO algorithm for the computation of buoyancy-driven flows. *Num. Heat Transf. B* **40**, 473–493.
- RUVINSKY, K. D., FELDSTEIN, F. I. & FREIDMAN, G. I. 1991 Numerical simulations of the

- quasi-stationary stage of ripple excitation by steep gravity–capillary waves. *J. Fluid Mech.* **230**, 339–353.
- SEIFFERT, B.R. & DUCROZET, G. 2018 Simulation of breaking waves using the high-order spectral method with laboratory experiments: wave-breaking energy dissipation. *Ocean Dynamics* **68**, 65–89.
- SEIFFERT, BETSY R., DUCROZET, GUILLAUME & BONNEFOY, FÉLICIEN 2017 Simulation of breaking waves using the high-order spectral method with laboratory experiments: Wave-breaking onset. *Ocean Modelling* **119**, 94–104.
- SHEMER, L., GOULITSKI, K. & KIT, E. 2007 Evolution of wide-spectrum unidirectional wave groups in a tank: an experimental and numerical study. *Eur. J. Mech. B/Fluids* **26**, 193–219.
- STIASSNIE, M. & SHEMER, L. 1984 On modification of zakharov equation for surface gravity waves. *J. Fluid Mech.* **143**, 47–67.
- STIASSNIE, M. & SHEMER, L. 1987 Energy computations for evolution of class i and ii instabilities of stokes waves. *J. Fluid Mech.* **174**, 299–312.
- STUHLMEIER, RAPHAEL & STIASSNIE, MICHAEL 2019 Nonlinear dispersion for ocean surface waves. *J. Fluid Mech.* **859**, 49–58.
- SUBRAMANYA, R. & GRILLI, S.T. 1994 Domain regridding in the computation of nonlinear waves. *Transactions on Modelling and Simulation* **9**, 139–150.
- TIAN, ZHIGANG, PERLIN, MARC & CHOI, WOORYOUNG 2008 Evaluation of a deep-water wave breaking criterion. *Phys. Fl.* **20**, 066604.
- TIAN, Z., PERLIN, M. & CHOI, W. 2010 Energy dissipation in two-dimensional unsteady plunging breakers and an eddy viscosity model. *J. Fluid Mech.* **655**, 217–257.
- TIAN, ZHIGANG, PERLIN, MARC & CHOI, WOORYOUNG 2012 An eddy viscosity model for two-dimensional breaking waves and its validation with laboratory experiments. *Phys. Fl.* **24**, 036601.
- TOFFOLI, A., DUCROZET, G., WASEDA, T., ONORATO, M., ABDOLAHPOUR, M. & NELLI, F. 2019 Ocean currents trigger rogue waves. In *Proceedings of the Twenty-ninth (2019) International Ocean and Polar Engineering Conference*, pp. 2453–2459.
- TOUBOUL, J., KHARIF, C., PELINOVSKY, E. & GIOVANANGELI, J.-P. 2008 On the interaction of wind and steep gravity wave groups using miles’ and jeffreys’ mechanisms. *Nonlin. Processes Geophys.* **15**, 1023–1031.
- VERON, FABRICE 2015 Ocean spray. *Ann. Rev. Fl. Mech.* **47**, 507–538.
- ZAKHAROV, V.E. 1968 Stability of periodic waves of finite amplitude on the surface of a deep fluid. *J. Appl. Mech. Tech. Phys.* **9**, 190–194.